

The Physical Parameters of Four WC-type Wolf-Rayet Stars in the Large Magellanic Cloud: Evidence of Evolution*

ERIN AADLAND,^{1,2} PHILIP MASSEY,^{2,1} D. JOHN HILLIER,³ AND NIDIA MORRELL⁴

¹*Department of Astronomy and Planetary Science, Northern Arizona University, Flagstaff, AZ, 86011-6010, USA*

²*Lowell Observatory, 1400 W Mars Hill Road, Flagstaff, AZ 86001, USA*

³*Department of Physics and Astronomy & Pittsburgh Particle Physics, Astrophysics and Cosmology Center (PITT PACC), University of Pittsburgh, 3941 O'Hara Street, Pittsburgh, PA 15260, USA*

⁴*Las Campanas Observatory, Carnegie Observatories, Casilla 601, La Serena, Chile*

ABSTRACT

We present a spectral analysis of four LMC WC-type Wolf-Rayet (WR) stars (BAT99-8, BAT99-9, BAT99-11, and BAT99-52) to shed light on two evolutionary questions surrounding massive stars. The first is: are WO-type WR stars more oxygen enriched than the WC-type stars, indicating further chemical evolution, or are the strong high-excitation oxygen lines in the WO-type stars an indication of higher temperatures. This study will act as a baseline for answering the question of where WO-type stars fall in WR evolution. Each star's spectrum, extending from 1100 Å to 25000 Å, was modeled using CMFGEN to determine the star's physical properties such as luminosity, mass-loss rate, and chemical abundances. The oxygen abundance is a key evolutionary diagnostic, and with higher resolution data and an improved stellar atmosphere code, we found the oxygen abundance to be up to a factor of 5 lower than previous studies. The second evolutionary question revolves around the formation of WR stars: Do they evolve by themselves or is a close companion star necessary for their formation? Using our derived physical parameters, we compared our results to the Geneva single-star evolutionary models and the BPASS binary evolutionary models. We found that both the Geneva solar metallicity models and BPASS LMC metallicity models are in agreement with the four WC-type stars, while the Geneva LMC metallicity models are not. Therefore, these four WC4 stars could have been formed either via binary or single-star evolution.

1. INTRODUCTION

Classical Wolf-Rayet stars (WRs) are the He-burning descendants of massive O-type stars. Their hydrogen-rich outer layers have mostly been stripped away, revealing the evolved core of the star. The spectra of WR stars are dominated by strong, broad emission lines formed in their optically thick stellar winds. WRs are split into two subtypes, the WN-type and the WC-type, based on their optical spectrum. The WN-type WRs show strong emission lines of helium and nitrogen (products of the earlier CNO-cycle H-burning), whereas the WC-type WRs show strong emission lines of carbon (products of He-burning via the triple-alpha process). A subcategory of the WC-type WRs, or a possible third subtype, is the WO-type WRs (first discussed in Barlow & Hummer 1982), whose spectra are similar to those of the WCs, except they have stronger high-excitation oxygen lines (i.e., O VI). These strong oxygen lines could be a product of further evolution, indicating the WOs are more evolved than the WCs. However, these lines could also suggest that the WOs have higher temperatures than the WCs, as that would result in the spectral oxygen lines strengthening as well.

The relation between the WC-type and WO-type WR stars can be determined by evaluating and comparing their physical parameters (luminosity, mass-loss rate, temperature, chemical abundances, etc.) using spectral modeling. This paper introduces the baseline to this study, by modeling and evaluating four WCs in the Large Magellanic Cloud (LMC). A follow-up study on a similar sample of LMC WO-type WRs is currently underway.

Corresponding author: Erin Aadland
aadlander@lowell.edu

* This paper includes data gathered with the 6.5 meter Magellan Telescopes located at Las Campanas Observatory, Chile.

Table 1. WC stars Observed

ID	Spectral Subtype	α_{2000}	δ_{2000}	V(mag)	M_V (mag)*
BAT99-8	WC4	04:56:02.89	-69:27:21.5	14.23	-4.7
BAT99-9	WC4	04:56:11.10	-66:17:33.06	14.33	-4.7
BAT99-11	WC4	04:57:24.08	-68:23:57.1	12.69	-6.0
BAT99-52	WC4	05:30:12.16	-67:26:08.3	13.53	-5.3

NOTE—* M_V has been corrected for extinction using the small reddening corrections determined in Section 4 and assuming a true distance modulus to the LMC of 18.5 (50 kpc).

All data except for M_V comes from [Neugent et al. \(2018\)](#) and references therein.

Already on its own, this study provides insight into the formation of WC-type WR stars. Yet, the stripping mechanism that exposes the core of a WR is undetermined. [Paczyński \(1967\)](#) proposed that all WR stars have binary companions which were responsible for stripping off the outer layers of the star. The ‘‘Conti scenario’’ ([Conti 1976](#)) argued that the mass-loss could be attained solely with stellar winds during earlier phases (i.e. O, Of) of evolution.

The importance of binarity for the formation of WR stars remains unknown. The frequency of short-period WR binaries in the LMC is roughly 30% ([Foellmi et al. 2003a](#)), similar to that in the Small Magellanic Cloud ([Foellmi et al. 2003b](#)), the Milky Way ([van der Hucht 2001](#)), and M31 and M33 ([Neugent & Massey 2014](#)). However, the drawback of using the binary frequency to answer the formation mechanism is that we do not know if the other 70% of WR stars were in binary systems that have since merged or if the binary companion is completely irrelevant in the stripping process. [Massey \(1981\)](#) compared the orbital separations of WR+O binaries and O-type binaries and found that mass transfer did not play an important role in WR evolution, but this study did not take into account mergers. [Sana et al. \(2012\)](#) evaluated O-type stars for binarity and found that 70% have a companion star, however, 1/3 of those will merge leaving their descendants to be single-stars.

In this study, we will be building off previous work analyzing WC stars by using significantly better observational data and a better analysis technique. Past analyses (see e.g. [Hillier & Miller 1999](#), [Grafener et al. 1998](#), [Crowther et al. 2002](#), [Barniske et al. 2006](#), [Sander et al. 2012](#)) have shown that WCs are carbon-rich ($\sim 40\%$ carbon mass fraction) and have determined values for their other physical parameters. Here, we will be using data obtained from the 6.5-m Magellan Baade telescope for the optical and near-Infrared wavelengths and data from the Hubble Space Telescope for the ultraviolet wavelengths. Our modeling will utilize the stellar atmosphere code CMFGEN, which is constantly being improved upon ([Hillier & Miller 1998](#), [Hillier 2003](#), [Hillier 2012](#)), and a tailored analysis, instead of a grid of models to give us unique physical parameters for each star and increased certainty in those values. This is particularly important in establishing the baseline for a comparison to the WO stars we will analyze in the subsequent study.

Our sample consists of four WC4s (BAT99-8, BAT99-9, BAT99-11, and BAT99-52) in the LMC (listed in Table 1). A radial velocity study by [Bartzakos et al. \(2001\)](#), found no signs of binarity for these four stars. We chose stars in the LMC over the Milky Way, since the distance to the LMC is accurately known, and since LMC stars typically have much lower reddening than Milky Way WC stars. A key result from our analyses, discussed separately in [Hillier et al. \(2021\)](#), is that BAT99-9 contains nitrogen.

In the next section, we discuss the observations utilized in this project. In Section 3, we discuss CMFGEN and the modeling process. The physical parameters of these stars are given in Section 4. The comparison to binary and single-star evolution models is in Section 5; our conclusions are provided in Section 6. In the Appendix, we address four concerns with our stellar atmosphere code and discuss the atomic data used in CMFGEN.

2. OBSERVATIONS AND REDUCTIONS

We obtained UV, optical, and NIR spectroscopic data for the four WC4 stars listed in Table 1, giving us coverage from 1100 Å through 25000 Å.

The UV observations, obtained with the Faint Object Spectrograph on the Hubble Space Telescope (*HST*), covered the wavelength region of 1140-3300 Å at a resolving power $R = \lambda/\Delta\lambda$ of 1100-1600. They were obtained using the G130H, G190H, and G270H gratings, with exposure times of 1500 s, 650 s, and 250 s respectively. The observations

were obtained on UT 1995 Nov 16 (data set Y2JE0403-7T), 1994 Sept 26 (data set Y2A10203-6T), 1996 April 15 (data set Y21E0105-8T), and 1995 Nov 21 (data set Y2JE0203-8T) for the stars BAT99-8, 9, 11, and 52, respectively. These UV observations were obtained as part of GO-5460 (PI: Hillier). The data were reduced using the standard reduction pipeline.

The optical data were collected using the Magellan Echellette (MagE; see [Marshall et al. 2008](#)) on the 6.5-m Magellan Baade Telescope at Las Campanas Observatory, covering the wavelength range 3150 to 9300 Å. The observations utilized the 1''0 slit yielding a resolving power $R = 4100$. Each observation consisted of three exposures with the star moved along the slit in order to improve the signal-to-noise. The slit was oriented to the parallactic angle. The BAT99-8 observations were taken on UT 2016 February 21 at a 1''0 seeing, an airmass of 1.4, and with 3×600 s exposures. BAT99-9 was taken on UT 2016 January 11 at a 0''7 seeing, an 1.7 airmass, and with 3×900 s exposures. BAT99-11 was taken on UT 2016 February 21 at a 0''89, an 1.4 airmass, and with 400 s exposures. BAT99-52 was taken on 2015 November 26 at 1''5 seeing, an airmass of 1.3, and with 3×300 s exposures. For each night of observing, some spectrophotometric standards were observed both at the beginning and end of the night. A ThAr arc was used for the wavelength calibration. For an in depth explanation of the reduction process, see [Massey et al. \(2014\)](#).

The NIR spectra were taken using the Folded port InfraRed Echellette (FIRE) on the Magellan Baade Telescope, for a wavelength range 8300 to 25000 Å. The 0''75 slit was used to obtain a spectral resolution of $R \sim 5000$. For the FIRE observations, four exposures are taken in a standard A-B-B-A pattern. BAT99-8, BAT99-9, and BAT99-52 were all observed on UT 2016 February 20, with BAT99-11 being observed the following night. The four stars had an average airmass of 1.5 and an average seeing of 0''9. The telluric standards, HD 40750, HIP 23252, HD 46630, and HD 40925, were observed using four 30 s exposures to make the telluric correction and use as a flux calibration for BAT99-9, BAT99-8, BAT99-52, and BAT99-11, respectively. These standards were observed directly after their corresponding WC star and at similar airmasses. A ThAr lamp was used to make wavelength calibrations and data reduction was done using the IDL FIRE pipeline ([Simcoe et al. 2013](#)).

For each of the four WCs, we combined the UV, optical, and NIR fluxed spectra with the latter two scaled. Both the optical and the NIR observations will suffer slit losses that may be larger or smaller than the spectrophotometric standards used for the flux calibrations, while the *HST* UV fluxes should be accurate at the 1-2% level. We therefore first scaled the optical spectra to the UV spectra by comparing the fluxes in the region of overlap, typically 3150-3300 Å. Similarly, the NIR spectra were then scaled to the rescaled optical in the region of overlap, typically 8300-9300 Å. We then combined the scaled spectra with the UV spectrum so that we had a single spectrum to work with. We estimate that this correction process is good at the 10% level or better, and is limited by the fact that the regions of overlap are always where the instruments are least sensitive and the calibration the poorest. We emphasize, however, that this scaling and combining was done purely for convenience; in doing the fits, we rescaled as needed when fitting a particular region. These rescalings were typically $\pm 7\%$, consistent with our expectations.

3. MODELING

Deriving the physical properties of WR stars is more complicated than generally true in stellar analysis work. The spectra of most stars consist of absorption lines that are formed in a relatively thin, hydrostatic layer, where the geometry can be assumed to be plane-parallel. Except for the hottest stars, and some unusual circumstances, local thermodynamic equilibrium (LTE) can be assumed. The outer layers of such stars are composed of $\sim 73\%$ (by mass) of hydrogen and 25% helium, with all other elements being a minor constituent by mass. Even for massive OB stars where line formation is affected by mass-loss from stellar winds, the process is simple relative to that of WR stars, with the surface gravity being determined from the pressure broadening of $H\gamma$, the effective temperature from the strengths of He I and He II lines ([Kudritzki & Simon 1978](#)), and the mass-loss rates from emission components of $H\alpha$ and He II $\lambda 4686$, with the stellar wind terminal velocity v_∞ (the velocity of the stellar wind far from the star where it is no longer accelerating) measured from the UV resonance lines (see, e.g., [Massey et al. 2013](#)). The luminosity then comes from the *V*-band photometry, after correction for reddening, distance, and after applying a bolometric correction based upon the temperature. The Stefan-Boltzman equation can then be used to determine the stellar radius, and, using the surface gravity, the stellar mass.

By contrast, the spectra of WR stars consist of mostly emission lines, which are formed in an optically-thick outflowing stellar wind. Mass-loss rates are typically an order of magnitude greater than that of even the most luminous O-type stars, and there is no such thing as a “photosphere.” Rather, high excitation lines are formed in

the inner part of the wind, while lower excitation lines are formed in the outer part of the wind¹ Further, the stellar “radius,” “surface gravity,” and “effective temperature” are no longer fundamental parameters since they depend on the properties of the stellar wind. One can still define the effective temperature using the radius of the star at a Rosseland optical depth of 2/3, but this is not easily related to the effective temperature defined by stellar evolutionary models. Alternatively, the above quantities can be well defined using a “core radius”, R_* , that represents the inner boundary of the stellar atmosphere where the expansion velocity is negligible (see, e.g., Hamann & Schmutz 1987, Schmutz et al. 1989). However, for many WR stars the “core radius” cannot be uniquely determined (Hillier 1991a; Najjarro et al. 1997; Hamann & Gräfener 2004).

The stellar wind velocity law is taken to be of the form

$$v(r) = v_\infty(1 - R_*/r)^\beta,$$

which is often referred to as the “Beta-law” (adapted from Castor et al. 1975). The value of β determines how steeply the wind is accelerating, with larger values being less steep. In general, a value of $\beta = 0.8$ seems appropriate for OB stars (although O super giants often have a $\beta > 1.0$), while $\beta = 1.0$ is taken for WR stars (Hamann & Schmutz 1987).

For WC stars, Hillier (1989) showed that the wind velocity undergoes a substantial increase at large radii ($r > 10R_*$), and that thus a two-component velocity law results in somewhat better fits, with the outer region having a very shallow slope ($\beta = 20$). In practice, $v_{\infty 1}$ in the inner region is found by fitting the line widths of the high-excitation lines (such as C IV), while $v_{\infty 2}$ in the outer region is found by fitting the line widths of the lower-excitation lines (such as C III). The two-component velocity-law has been widely adopted by the massive star community, following the work of Gräfener & Hamann (2005). Their hydrodynamic model showed that a two-component model was a good approximation. More recently, Sander et al. (2015) used a method by which the velocity field was constantly updated by integrating the hydrodynamic equation for both inwards and outwards from the sonic point.

The situation in terms of abundances is also complicated. For many WN-type WRs a reasonable first approximation is that the surface composition is helium with little or no hydrogen, with most of the initial carbon and oxygen tied up in the form of nitrogen, in accord with our expectations of CNO-equilibrium abundances. For most other species, standard abundances, can be adopted.

For WC-type WRs the situation is far more complicated, since He-burning has produced carbon, giving it an abundance comparable to that of He. The mass-fraction of carbon is dependent on the degree of chemical evolution, and has to be determined concurrently with the other stellar parameters. Furthermore, as carbon is built up in the core, helium and carbon will combine to produce oxygen, and potentially its abundance also has to be determined concurrently with the other stellar parameters.

3.1. CMFGEN

In order to model the stellar atmospheres of WC stars, a radiative transfer code that uses non local-thermodynamic-equilibrium (non-LTE) and line blanketing for extended, outflowing atmospheres is required. CMFGEN (“Co-Moving Frame GENeral,” Hillier & Miller 1998) accomplishes this and was used to model the four WC stars. The CMFGEN input parameters that we adjusted during our analyses are the luminosity, the terminal velocity of the wind and its shape, the mass-loss rate, and the chemical abundances of helium, carbon, and oxygen.

Determining the best values for each parameter was done using a tailored analysis. This approach entails finding the best values by running model after model, altering the parameters and improving the fit until we have converged on a model with excellent agreement to the observed spectrum (as our group has done in the past, see e.g., Hillier 1989, Hillier & Miller 1999). While this process takes longer than using a grid of models, it allows the model to be changed uniquely for each star to find the best values for each parameter. It also allows us to evaluate more parameters than would be possible using a grid.

CMFGEN has also evolved throughout the years (Hillier & Miller 1998, Hillier 2003, Hillier 2012) leaving a more accurate stellar atmosphere code than what has been used in previous studies of WR stars, by incorporating improved atomic data, using a two-component velocity law for WC stars, and in an improved treatment of clumping, to name just a few refinements.

¹ The line-formation mechanisms have been extensively discussed by Hillier (2015).

3.2. Fitting the Observed Spectrum

Fitting the spectra of the WC-type stars is often a balancing act between all of the physical parameters. This is due to the spectral lines being influenced by multiple parameters, e.g. luminosity, mass-loss rate, temperature, and chemical abundances. Further, most of the lines are blended, consisting of a combination of carbon, helium, or oxygen, such as all of the He II lines are blended with carbon lines. CMFGEN may also contain errors in the atomic data which will influence the fit quality. All of these things result in lines of the same species and ionization states not being equally well fit using a single set of parameters. Thus, compromises are made during the process to obtain the best fit model.

In our WC spectra the continuum is masked by the rich emission line spectrum and this makes normalizing the spectrum futile. Therefore, we did our fitting without normalization, utilizing fluxed spectra. In order to allow for small differences in the fluxing from the UV, optical, and NIR, the models were relatively scaled to three regions where there are no emission lines to determine if the model fits the observed spectrum. The UV, optical, and NIR model spectra were scaled using the relatively line-free regions from 1740-1780 Å, 6000-6100 Å, and 15100-15200 Å, respectively. When the scaling needed to be adjusted for large differences in the flux between the spectrum and the model, absolute scaling was done by adjusting the mass-loss rate, radius, and luminosity such that $\frac{\dot{M}^2}{R_*^2} = \text{constant}$ and $L \propto T_{eff}^4 R_*^2$.

The modeling process begins with finding reasonable values for the luminosity and the mass-loss rate. Both are primarily determined by the continuum and all of the emission lines. However, more explicitly, since the temperature and thus luminosity are tied to the distance at which lines form in the wind, the luminosity can be determined using the ionization ratios, e.g. C IV/C III, O V/O IV/O III, and He II/He I. We found that the C III $\lambda 9710$ line's flux was particularly useful in determining the luminosity. Similarly, the flux of the He I $\lambda 10830$ is sensitive to the mass-loss rate of the star and can be used to further constrain its value. The model is not sensitive to the given radius of the star (see Appendix A) and is thus only altered to adjust the absolute scaling.

It is well known that the winds of WR stars are clumped (e.g., [Owocki et al. 1988](#); [Hillier 1991b](#), [Robert 1994](#); [Crowther et al. 2002](#)). Typically in CMFGEN we assume that there is no interclump medium, and describe the clumping using the volume-filling factor, “f” which has the form

$$f = f_\infty + (1 - f_\infty) \exp(-V/V_{cl}) \quad (1)$$

where f_∞ is the volume-filling factor at large radii, and V_{cl} is an onset onset velocity (see Section C in the Appendix). The above formula is not based on any physics – it is simply a convenient formulation, and other formulations could easily be adopted. For our analyses, f_∞ was typically set to 0.05. From the spectra, uniform clumping values of 0.2 and higher are found to be incompatible with the red-wings seen on many emission lines (Appendix B and C). However, constraining f_∞ is difficult, and it is also probable that our simple prescription does not adequately describe the run of $f(r)$ in the wind.

The velocity law terminal velocities were determined using line widths. The two-component velocity law used in CMFGEN requires us to use different lines for each component. In the inner region, where the temperature is the hottest, the terminal velocity component, $V_{\infty 1}$, is best determined using lines from moderate ionization species, such as C IV and He II, and which account for the majority of the lines in the WCs' spectra. After a general analysis of all of the high excitation lines in the spectrum, we used the width of C IV $\lambda\lambda 5801, 12$ to refine the terminal velocity of the inner component. For the outer region component, $V_{\infty 2}$, we used lines from “low” ionization species whose emission lines are formed in the outer region of the star's wind. The lines we primarily used were C III $\lambda 2289$, C III $\lambda 9710$, and He I $\lambda 10830$. The β values were kept constant, with the outer component being set to $\beta = 20$ and the inner component being set to $\beta = 1.0$.

The chemical abundances of helium, carbon, and oxygen were found using corresponding emission line strengths and line ratios. The line strengths of the emission lines are not only contributed to by the chemical abundance but also by luminosity (affects the C III to C IV and He I to He II line strengths), mass-loss (affected He I $\lambda 10830$) and temperature (affects the C III to C IV and He I to He II line strengths). In Fig 1, a WC model has been split into the different atomic species that contribute to the complexity of the spectrum. Most lines in the WCs' spectra are blended lines with He contributing to some C lines and visa versa (for example, the He II $\lambda 4686$ line has C IV $\lambda 4683$ and C III $\lambda 4673$ contributing to it). The atomic species that formed the CMFGEN model are discussed in Appendix E.

Therefore, once the line strengths are roughly correct from the four parameters, the relative abundances of carbon and helium are found using line ratios of C/He, C IV $\lambda 2698$ /He II $\lambda 2733$, C IV $\lambda 5473$ /He II $\lambda 5411$, and C IV $\lambda 11905$ /He II

$\lambda 11626$. In some cases (e.g. C IV $\lambda 11905$ /He II $\lambda 11626$) both lines tended to be systematically too strong; however, we assume that the ratio is still reflective of the relative abundance. The oxygen abundance, on the other hand, was determined using the relative strength of the oxygen lines, primarily O VI $\lambda 5291$ and O V $\lambda 5596$.

For the reddening determination, we adopted a CMM law (Cardelli et al. 1989) for the foreground component and a Mathis law for the LMC component (Howarth 1983). The Galactic foreground reddening law was set with values of $R=3.1$ and $E(B-V)=0.08$ mags (Cardelli et al. 1989). We then fit the LMC component, finding $E(B-V)$ values 0.03-0.08 mags. We assumed a distance of 50 kpc for the LMC (van den Bergh 2000, Pietrzyński et al. 2019).

The spectral fits to each star are shown in Figures 2-5. To emphasize both the complexity of the spectra, and the futility of trying to normalize the spectra, we also show the “true” continuum of the model.

These model fits are representative of the WC stars, with the models matching even the low flux spectral features. This is especially impressive as the models were adjusted to best fit the emission lines with the strongest fluxes. The low flux emission features were analyzed last as a mere check for final agreement and parameters were only adjusted slightly for them. The end result was a model that replicated almost every feature in the WC spectrum from their strength and shape. The agreement of the small emission features shows the accuracy and capabilities of CMFGEN.

The models also reproduced the line widths of both the low and high excitation emission lines. This was due to the two-component velocity law that enabled us to calibrate each component for the excitation lines separately.

Each of the stars’ corresponding model has features that agree particularly well. In BAT99-9 and BAT99-11’s models the oxygen lines, O VI $\lambda 5291$ and O V $\lambda 5596$, are in agreement with their spectrum line strength to within a factor of 1.05. BAT99-9 and BAT99-52 have a fit to within a factor of 1.1 for C III $\lambda 2289$, which was a difficult line to fit in BAT99-8 and BAT99-11 (factors of 1.3 off). All of the models have a nice fit on the blend line of C IV $\lambda 4683$ and He II $\lambda 4686$ (factor of 1 to 1.2 different) and/or the C IV $\lambda \lambda 5801,12$ blend line (up to a factor of 1.2 different).

For the models, there were also some common problems. For example, the O IV $\lambda 3400$ line is too high in all of the models, in some cases by a factor of 2. The C IV $\lambda 20700$ line is consistently too high. The C III lines, $\lambda 2289$, and $\lambda 9710$, had to be balanced as $\lambda 2289$ was typically too high and $\lambda 9710$ was typically too low. This discrepancy can be attributed to a combination of errors in the atomic data and slight errors in the models.

The O VI $\lambda \lambda 3811,3834$ doublet has additional issues in the models. This doublet is an important feature that separates the WCs from the WOs. The doublet is consistently too low in the models. This may be an affect of the clumping due to the ionization structure of the line. The line is formed deeper in the stellar wind, meaning that the clumping of the models may be interfering with the photons making it to the surface. Appendix D includes an in-depth discussion on the inability to fit the O VI $\lambda \lambda 3811,3834$ doublet.

3.3. Chemical Abundance Uncertainties

The chemical abundance uncertainties for the C/He ratio and O were determined by adjusting their values to find the limits where the fits would no longer be acceptable. The C/He ratio uncertainty was determined using the He II and C IV line pairs and referencing the He I $\lambda 10830$ and C III $\lambda 9710$ lines. This was found by changing the carbon and helium abundances of the best fit model for each star and leaving all other parameters fixed. Once the line ratios were no longer representative of the line pairs (e.g. the line strengths became even or flipped), the uncertainty was called. The oxygen was altered in a similar way, where the O VI $\lambda 5291$ and O V $\lambda 5596$ (with a significant O III contribution) lines were used to determine the realistic uncertainty. The lower and upper oxygen uncertainties were established once the oxygen lines in the model were no longer fitting the oxygen lines. These models showing the limits of acceptable values for the C/He abundance are shown in Figure 6 and for the oxygen abundance in Figure 7. The uncertainty values for the chemical abundances are listed in Table 2.

The oxygen abundance was also given a larger “generous” uncertainty to check the limits of oxygen in one of the stars (BAT99-8). The lower limit was determined by fitting the O IV $\lambda 3400$ line, as all of the stars’ best fit models were too high for this line. However, by reducing the oxygen abundance to fit the O IV $\lambda 3400$ line, all other oxygen lines in the model became too low to be reasonable fits to the spectrum. The upper limit for the “generous” oxygen uncertainty was found by making all of the oxygen lines high in the model compared to the spectrum. This is also unreasonable for the actual oxygen abundance for the WC star. Therefore, the generous uncertainty describes the possible range of oxygen, but not a reasonable range of oxygen for the star. A model with an oxygen abundance at either of these bounds would not be a good fit to the spectrum and instead is used as a check on what the extent of oxygen could be in the star. The resulting generous uncertainty for BAT99-8 was $0.077^{+0.13}_{-0.037}$.

3.4. Hidden Companions

The four stars analyzed here were selected as none show signs of having a binary companion. None show either the radial velocity variations (Bartzakos et al. 2001) or any spectroscopic sign of a companion (Bartzakos et al. 2001; Neugent et al. 2018). Nevertheless, as the late Virpi Niemela would remind us, one can only prove that a particular star *is* a binary, never that it is single. The orbital inclination may be unfavorable for radial velocity variations, or the companion might be too faint to detect spectroscopically. We were therefore interested in understanding what sort of companion could have escaped our notice.

To address this, we utilized the TLUSTY BSTAR2006 (Lanz & Hubeny 2007)² and Phoenix (Husser et al. 2013)³ models. We considered the possibility that our spectra were actually blends of WC4 stars plus a main-sequence companion star ranging from B0 V to A0 V. For this experiment we considered companion stars of spectral types B0 V ($M_V = -4.0$, $T_{\text{eff}} = 28,000$ K, $18M_{\odot}$), B2 V ($M_V = -2.5$, $T_{\text{eff}} = 18,000$ K, $10M_{\odot}$), B5 V ($M_V = -1.2$, $T_{\text{eff}} = 14,000$ K, $6M_{\odot}$), B8 V ($M_V = -0.3$, $T_{\text{eff}} = 11,000$ K, $4M_{\odot}$), and A0 V ($M_V = +0.7$, $T_{\text{eff}} = 10,000$ K, $3M_{\odot}$), with the values drawn from Cox (2000) and Humphreys & McElroy (1984). The corresponding $\log g = 4.0$ models at LMC-metallicity were rotationally broadened to 75 km s^{-1} , and their fluxes scaled to the expected M_V . The model spectra were then reddened using a CMM law with an $E(B - V) = 0.13$, typical of what we find for our SED fitting (Section 5) and the LMC in general (Massey et al. 2007). We then subtracted the reddened models from our spectra and examined the resulting spectra. We found that the observations could easily hide an A0 V or a B5 V star, but that a companion of spectral type B2 V or earlier would distort the even-N Pickering He II lines due to the strong hydrogen lines present in the B stars. Thus, we would be blind to any stellar companion with a mass of $\sim 8M_{\odot}$ or lower.

We will also note that a close compact companion (neutron star or black hole) would also go undetected if the orbital inclination was seen pole-on. However, a Vizier search does not find any of these stars associated with X-ray sources, suggesting that none of these stars has a close compact companion. It is possible that the stars could be in a wide orbit binary, in which case the X-ray source may not be detected (Eldridge et al. 2020). Another option is that the X-ray emission from the companion is weak; this could occur if the companion is a black hole without an accretion disk (Schootemeijer & Langer 2018).

4. PHYSICAL PARAMETERS

The physical parameters determined by our fits are summarized in Table 2, along with corresponding values from Grafener et al. (1998) and Crowther et al. (2002). The four WC stars have mass-loss rates that vary by a factor of 2.7. Similarly, the luminosity of the stars differs by a factor of 2.4. The chemical abundances are closer in value, with helium changing by a factor of 1.53 between the stars, carbon differing by a factor of 1.68, and oxygen being a factor of 2 different.

While evaluating the four WC stars, we discovered three emission features in BAT99-9’s spectrum that were not in the other WC stars’ spectra, specifically, N V $\lambda 1240$, N IV $\lambda 1718$, and N IV $\lambda 3480$. These lines were fit by introducing nitrogen into the model (0.00095 by mass). This is the first discovery of nitrogen in a WC star, and the implications are discussed further in Hillier et al. (2021).

4.1. Comparison with Previous Work

The four WC-type stars analyzed here were also modeled by Grafener et al. (1998) and Crowther et al. (2002). Grafener et al. (1998) used the Potsdam Wolf-Rayet Models (PoWR, Gräfenner et al. 2002) and Crowther et al. (2002) utilized CMFGEN (Hillier & Miller 1998). However, the models utilized in Grafener et al. (1998) were not fully blanketed; i.e., the models did not account for blanketing by the iron group elements.

In terms of the helium abundances, we find similar values to those found by Crowther et al. (2002) with all differences $< 10\%$.

In terms of the carbon abundances, we find similar values to Crowther et al. (2002), with an agreement of 15% or lower, but with larger differences with Grafener et al. (1998). BAT99-8 and BAT99-52 have carbon abundances that have an agreement within 5% to Grafener et al. (1998), but for BAT99-11, Grafener et al. (1998) has an abundance that is a factor of 2 larger. The carbon abundance is in agreement with the limit proposed by Higgins et al. (2021),

² <http://tlusty.oca.eu/Tlusty2002/tlusty-frames-BS06.html>

³ <http://phoenix.astro.physik.uni-goettingen.de>

Table 2. Physical Parameters

ID	$\log \dot{M}$	$\log(L/L_{\odot})$	$R_{2/3}$	T_{eff}	f	$\log \dot{M}/\sqrt{f}$	X(He)	X(C)	X(C)/X(He)	X(O)	X(Ne)	E_{B-V}^{LMC}	$V_{\infty,1}, V_{\infty,2}$	Ref ⁴
			R_{\odot}	kK								mags	km s^{-1}	
BAT99-8	-4.84	5.48	2.4	87	0.05	-4.2	0.50	0.41	$0.83^{+0.25}_{-0.08}$	$0.077^{+0.063}_{-0.017}$	0.011	0.05	1600, 2600	
	-4.06	5.13	6.46	43.6	-		-	0.4		0.3	-	0.06	2300	G98
	-4.9	5.42	3.4	71	0.1		0.45	0.47		0.08	-	-	2300	C02
BAT99-9	-4.85	5.48	2.6	84	0.05	-4.2	0.66	0.29	$0.43^{+0.13}_{-0.04}$	$0.041^{+0.037}_{-0.008}$	0.011	0.08	1600, 2300	
	-4.16	5.29	5.94	49.8	-		-	0.4		0.2	-	0.08	2300	G98
	-4.8	5.44	3.2	74	0.1		0.65	0.25		0.10	-	-	2500	C02
BAT99-11	-4.42	5.86	5.5	72	0.05	-3.8	0.72	0.25	$0.34^{+0.11}_{-0.03}$	$0.025^{+0.023}_{-0.0050}$	0.011	0.06	2100, 3000	
	-3.80	5.62	10.4	45.6	-		-	0.5		0.2	-	0.05	2800	G98
	-4.5	5.70	5.2	67	0.1		0.66	0.28		0.05	-	-	3000	C02
BAT99-52	-4.70	5.65	3.3	83	0.05	-4.0	0.47	0.42	$0.90^{+0.27}_{-0.09}$	$0.094^{+0.076}_{-0.017}$	0.011	0.03	1800, 2600	
	-3.91	5.26	8.03	42.1	-		-	0.4		0.3	-	0.01	2600	G98
	-4.5	5.65	4.8	68	0.1		0.46	0.44		0.09	-	-	2900	C02

NOTE— ¹ $R_{2/3}$ and T_{eff} are defined at a Rosseland optical depth of 2/3.

² Determined using a foreground reddening component $E(B-V)=0.08$ plus the LMC component listed here.

³ We used a two-component velocity law, while the previous studies used a one-component law.

⁴ References: G98 - Grafener et al. (1998); C02 -Crowther et al. (2002)

in which a WC star can only ever reach a carbon mass fraction of 50% regardless of the amount of stripping taking place (shown in Figure 5 of their text).

The biggest difference between these previous studies and ours is the oxygen abundance. Our values are similar to Crowther et al. (2002) for two of the stars (BAT99-8 and 52), but half as large for BAT99-9 and 11. Our values are a factor of 3 to 5 smaller than those of Grafener et al. (1998). The oxygen abundance is one of the most important values in our study due to the main difference between the WCs and WOs being an O VI line.

The difference between these two sources and our results may be due to the improvements in our stellar atmosphere code and atomic data over the last two decades or our exceptional spectra data set.

Finally, we compare our results with the general findings of Sander et al. (2012), who analyzed a sample of Galactic WC stars, ranging in spectral subtype from WC4 to WC9⁴. There are three WC4 stars in their sample; we find luminosities are considerably higher ($\log L/L_{\odot}=5.5-5.9$) than those in their sample ($\log L/L_{\odot} = 5.1 - 5.2$) even when corrected for revised distances from Gaia (Sander et al. 2019). Our mass-loss rates range from $\log \dot{M}/\sqrt{f}=-3.8$ to -4.2 ; theirs are very similar, ranging from -4.1 to -4.3 . They did not actually adjust their fits for abundances, but rather adopted a carbon mass fraction of 40%, 55% for helium, and 5% for oxygen. This can be compared to our derived values in Table 2, where the mass fraction of carbon ranges from 25% to 42%, that of helium ranges from 47% to 72%, and that of oxygen range from 2.5% to 9.4%. In Sander et al. (2012)’s Appendix, WR52 and WR144 were modeled using a higher oxygen mass fraction of 15% with a carbon mass fraction of 50% and a helium mass fraction of 35%. Similar to our models, even with a higher oxygen abundance the O IV $\lambda\lambda 3811, 3834$ doublet was still not able to be reproduced (remaining too low in the models). We expect that as nuclear burning proceeds that the carbon and oxygen abundances will increase at the expense of helium, and that shall find in the next section that our abundance determinations serve as a powerful tool for diagnosing the evolutionary status of these stars.

5. COMPARISON TO EVOLUTIONARY MODELS

An important part of our study is to find out what we can learn about the evolution of these stars by comparing their physical properties to those predicted by stellar evolutionary models. For this task, we used the “Binary Population and Spectral Synthesis” (BPASS) models (Eldridge et al. 2017) and the Geneva single-star evolutionary models (Ekström et al. 2012) to determine if our results are in agreement with either type of evolution. For BPASS, the LMC metallicity ($Z=0.006$) binary models were used; while the BPASS models contain single star evolutionary models as well, these were only used as a check and not in our evaluation. We used the Geneva models that included rotation computed for metallicities of $Z=0.006$ (P. Eggenberger, 2021, in prep.) and $Z=0.014$ (Ekström et al. 2012). Although the former is closer to the metallicity of the LMC ($Z=0.007$), the higher metallicity models also proved very useful for comparison, as they have higher mass-loss rates during the main-sequence phase. This allows us to evaluate evolutionary tracks with a wider variety of mass-loss rates, in addition to accounting for uncertainties in the mass-loss evolutionary models’ calculations.

For the comparison to the WC star sample, we only used the evolutionary models that had a WC phase according to the limits used by Georgy et al. (2012), $X_{\text{H}} < 0.3$ and $\log(T_{\text{eff}}) > 4.0$, and the standard requirement for the WC-type stars that $C > N$. Binary stripping can produce hot stars with the expected surface chemical compositions as WRs, but whose luminosities are too low to develop the optically-thick stellar winds that are needed for a star to be identified as a WR (e.g. Sander et al. 2020, Shenar et al. 2020). Thus, typically a luminosity limit of $\log L/L_{\odot} > 4.9$ is further proposed. This is an issue for WN-like stripped binaries, but not for WCs, in that none of the BPASS models that met the other criteria had luminosities less than $\log L/L_{\odot}=5.2$. The authors made use of a python package called *hoki* (Stevance et al. 2020) to aid in the process of reading the BPASS models.

5.1. Chemical Abundances

In Fig. 8, the WC stars’ mass fractions of helium, carbon, and oxygen are compared to those of the evolutionary models. As a WC star evolves, we expect that the carbon will increase and the helium will decrease as a result of the triple-alpha process. As the carbon abundance increases, oxygen will be created as helium and carbon combine. This is shown in the evolutionary tracks of the Geneva single-star and BPASS binary models. The measured chemical abundances for the four WC stars fall directly on both the BPASS and Geneva evolutionary tracks. Moreover, the

⁴ This landmark paper was the first to use fully blanketed models to analyze a set of WCs, but did suffer from several unavoidable problems. One difficulty with such Galactic studies, particularly in the pre-Gaia era, was the uncertainties in distance and hence the derived luminosities. Furthermore, the typically high Galactic reddening precluded UV observations of many of their targets. Finally, their optical data relied upon the Torres & Massey (1987) spectrophotometry, which, although the best achievable in the pre-CCD era, suffered from linearity issues for many of the stronger lines, as we have found in comparing our modern data to theirs.

chemical abundances of BAT99-8 and BAT99-52 indicate that they are more chemically evolved than BAT99-9 and BAT99-11.

In Fig. 9, we compare the measured surface abundance ratios with those predicted from the models. Except for the $60 M_{\odot}$ $Z=0.006$ model, the Geneva models predict a tight relationship between the O/He and C/He ratios, as would be expected for single-star evolution. Our results fall along this sequence. By contrast, the BPASS binary models show a large range of O/He values for a given C/He ratio.

The BPASS models, while spanning a larger range of O/He values, do have some that fall near our observed values. The span of BPASS models could be due to binary interactions extending or changing the time of the helium burning to produce more oxygen in those stars. Total, the BPASS models have around 3000 models that produce WC stars based on our cutoffs. About a third (1133) of these models are in the region populated by the four WC stars studied here. In this smaller region half the models have a companion star that has merged or is no longer visible (fainter than M_V of -1 mag). We can split this region up further by looking at WC masses that are greater and smaller than $21 M_{\odot}$. The models with primary stars less massive than $21 M_{\odot}$ are the models closest to the four WC stars analysed here (BAT99-8, BAT99-9, BAT99-11, and BAT99-52), totalling 282 models with 185 models having faint companions.

5.2. Luminosity

In Fig 10, we compare our values for the luminosities and surface abundances with the evolutionary models. The luminosities of the $Z=0.006$ Geneva models do not extend as low as what we have for the observed stars. However, there is good agreement with the higher metallicity $Z=0.014$ Geneva models. Although BAT99-8 and -9 are of lower luminosities than the lowest mass Geneva model that still produces a WC star ($40 M_{\odot}$ solar metallicity model), this is likely a limitation of the large gaps between mass tracks, i.e., the models displayed here differ by at least $20 M_{\odot}$. It is possible that a $35 M_{\odot}$ model would produce a WC star with a lower luminosity needed for BAT99-8 and BAT99-9.

The BPASS models produce WC stars with luminosities extending down to those of the WC stars. The region of BPASS models near the stars in the chemical abundance parameter space also span a region between $\log(L/L_{\odot}) = 5.3 - 6.4$ dex. This indicates that those models could produce the four WC stars studied here.

There are no WC-type stars formed from either the Geneva or the BPASS models below $\log(L/L_{\odot})$ of 5.2 dex. In the LMC, we have not observed any WC-type stars that have lower luminosities, therefore, this lower limit in the evolutionary models is in agreement with reality.

The luminosity has also been compared to the current WC masses of the Geneva and BPASS evolutionary models as seen in Fig 11. The evolutionary tracks of the Geneva models and BPASS models have the same luminosity-mass relation. The selected BPASS models in the region similar to our chemical abundance parameter space are in agreement with the solar metallicity Geneva models. This suggests that, the physical parameters of WC stars are independent of how they formed.

5.3. Lifetimes

The chemical abundance ratios vs. time before the star goes supernova is shown in Fig 12. According to both the Geneva and BPASS models, the chemical abundances of the WC stars can be achieved at one-third of the WCs' lifetime for BAT99-9 and 11 and at about two-thirds of the WCs' lifetime for BAT99-8 and 52. The time (before the star goes supernova) at which the stars' C/He and O/He agree with the Geneva evolutionary models occur at roughly the same time: 0.13 Myr, 0.14 Myr, 0.17 Myr, 0.18 Myr for BAT99-52, BAT99-8, BAT99-9, and BAT99-11 respectively. This is also true for the BPASS models which happen within a few hundredths of a Myr from the time the Geneva models match. The time at which these chemical abundances occur in the models indicates that both sets of models can predict the observed chemical abundances for a WC star. The length of time for each of these models to have the observed chemical abundances is also reasonable.

5.4. Mass-Loss Rates

The mass-loss rates assumed by the evolutionary BPASS and Geneva models are consistent with those determined for the four WCs given our clumping factor, shown in Fig 13. When the mass-loss rate is compared with the luminosity, the stars are in agreement with the Geneva solar metallicity models, except the $85 M_{\odot}$ model. The BPASS models with similar chemical abundances to the four WC stars have a wide range of mass-loss rates, but most fall in the region with mass-loss rates and luminosities comparable to the four WC stars.

The C/He ratio compared to the mass-loss rate shows excellent agreement for BAT99-11 which falls between the Geneva solar metallicity models. The other WC stars have mass-loss rates that are lower than what the Geneva models

have for their C/He abundances. However, a slightly lower mass Geneva model would take into account BAT99-52 position and possibly BAT99-8 and BAT99-9. The BPASS models are in excellent agreement with the WC stars. While, the Geneva models do not correspond with two of the WC stars, this is not enough to rule out single-star formation for WC stars.

6. SUMMARY AND CONCLUSIONS

In this paper, we have derived physical parameters for four apparently single WC stars in the LMC: BAT99-8, BAT99-9, BAT99-11, and BAT99-52. We have compared these properties to those predicted both by the Geneva single-star models and the BPASS binary models.

We find a significant lower oxygen abundance than found by previous studies of these four stars (Grafener et al. 1998, Crowther et al. 2002). The explanation for this difference may be that we used higher resolution data and an improved stellar atmosphere code. The oxygen abundance is significant for determining how these stars evolved and the relation between WC and WO stars.

Both sets of Geneva models do a good job of matching the surface abundances of the WC stars. However, the lower metallicity models, $Z = 0.006$, do not predict WC stars with as low luminosities as what we observe, despite being a better match to the metallicity of the LMC. This is likely due to the difference in the adopted mass-loss rates during the evolution of these stars. One explanation for this could be that the Geneva models assume a stable mass-loss rate, while in actuality these stars may also experience mass-loss through eruptions. These eruptions would mean that the Wolf-Rayet stars are undergoing more mass-loss than the Geneva models account for. We should also keep in mind that although the oxygen abundance of the gas in the LMC is well determined, the overall metallicity is not set in stone, as the $Z = 0.007$ value assumes scaling of solar abundances, which themselves have been a matter of debate (Asplund et al. 2005, Asplund et al. 2009).

The BPASS models span an expansive range in chemical abundances, luminosities, and star masses. However, only a third of the BPASS models that produce a WC star have similar chemical abundances to the observed WC stars. The BPASS models in this region have reasonable luminosities, timescales, mass-loss rates, etc. for the WC-type stars and half of them no longer have a companion star or have a faint companion.

From our comparisons of the WC stars' physical parameters to both the Geneva single-star and the BPASS binary evolutionary models, we found that these stars are in a parameter space compatible with models from both types of evolution. In fact, it may not matter how WC-type stars lost their mass as both types of evolutionary models have the same luminosity-mass relation.

The next step in this study is to model our sample of WO-type stars and compare their physical parameters with those found here for the WC-type stars. This upcoming study will allow us to assess if the WO-type WR stars are more chemically evolved than WC-type stars or are at a similar stage of evolution.

ACKNOWLEDGMENTS

Northern Arizona University and Lowell Observatory sit at the base of mountains sacred to tribes throughout the region. We honor their past, present, and future generations, who have lived here for millennia and will forever call this place home. The optical and NIR spectra used in this study were obtained at Las Campanas Observatory (LCO), and we are grateful to the continued support of the Carnegie and Arizona Time Allocation Committees for our work. We are also grateful to the excellent support and technical assistance we also receive at LCO. This work was partially supported through the NASA/ADAP grant 80NSSC18K0729, through the National Science Foundation grant AST-1612874, and through the STScI grant HST-GO-13781. Computer resources were also supported through a Slipher Society award. EA would like to acknowledge the gracious support of her Lowell Pre-doctoral Fellowship by the BF Foundation. We also thank Kathryn Neugent for help both with some of the observing proposals and for taking some of the data used here. The authors are grateful to Jan Eldridge and Andreas Sander for useful suggestions on a previous version of this manuscript. We thank our anonymous reviewer for the helpful feedback on our paper.

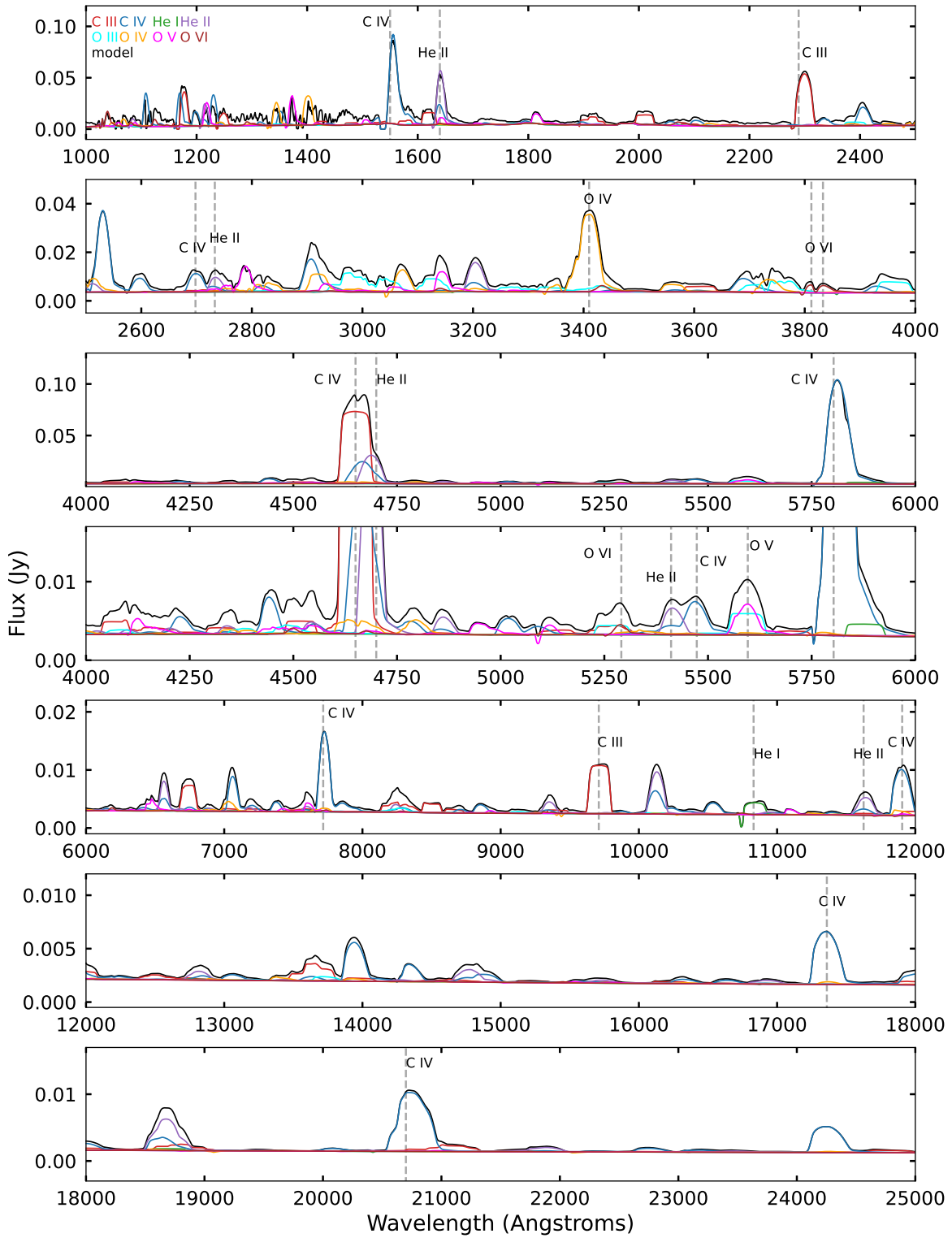


Figure 1. Atomic species in BAT99-8's Model. The main composition of the model's spectrum (black) features are He I (green), He II (purple), C III (red), C IV (blue), O III (cyan), O IV (orange), O V (magenta), and O VI (brown). Most of the lines in a WC star's spectrum are blended as can be seen with all of the atomic species contributions in the model separated out.

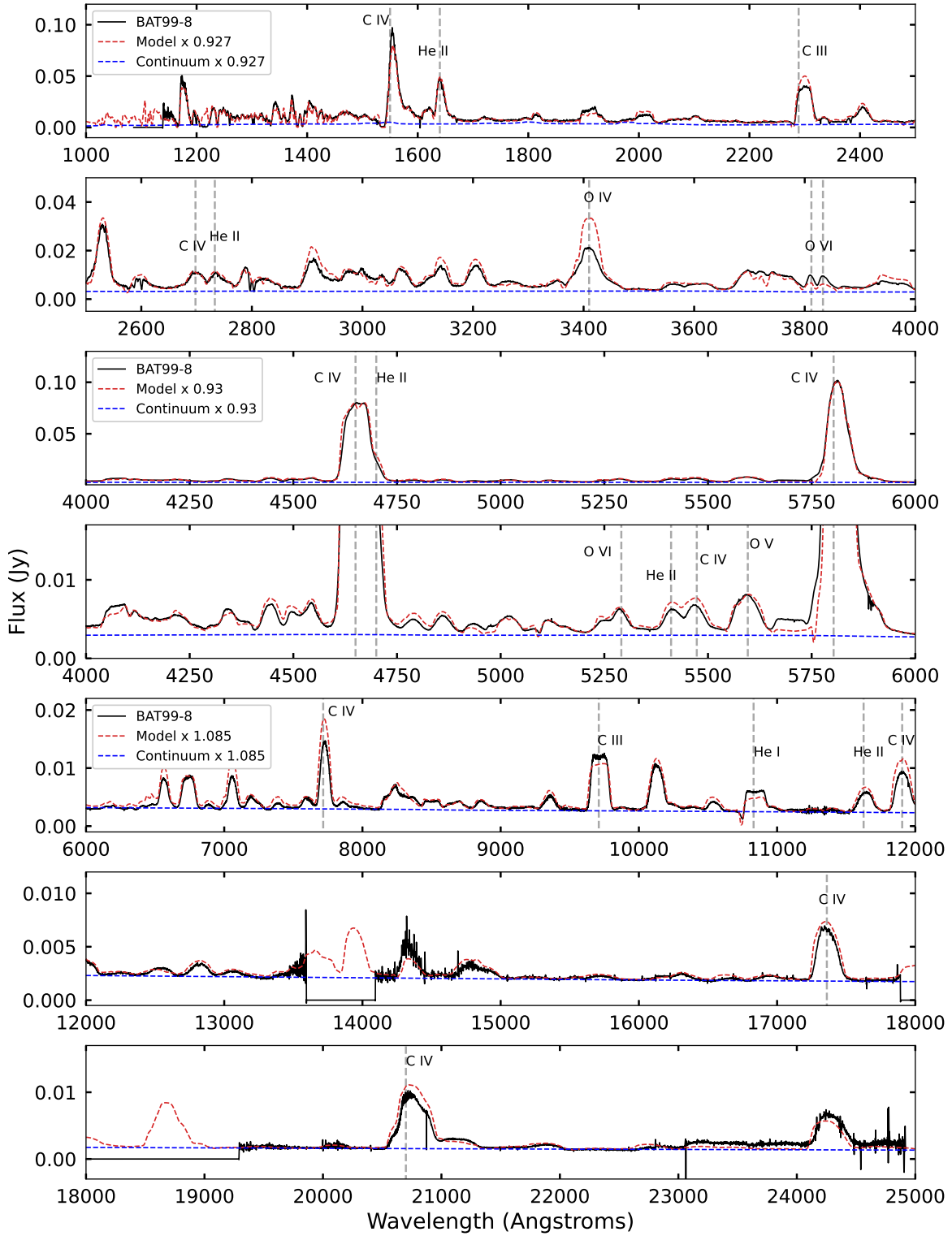


Figure 2. The observed spectrum of BAT99-8 (black) with the best fit model (red dashed) and the model's continuum (blue dashed). The model was scaled to the spectrum's continuum. The labeled emission lines are those primarily used for modeling the spectrum. The current disagreements in the model being too high for O IV λ 3400 and too low for O VI λ 3811,3834 may be due to atomic data issues in CMFGEN.

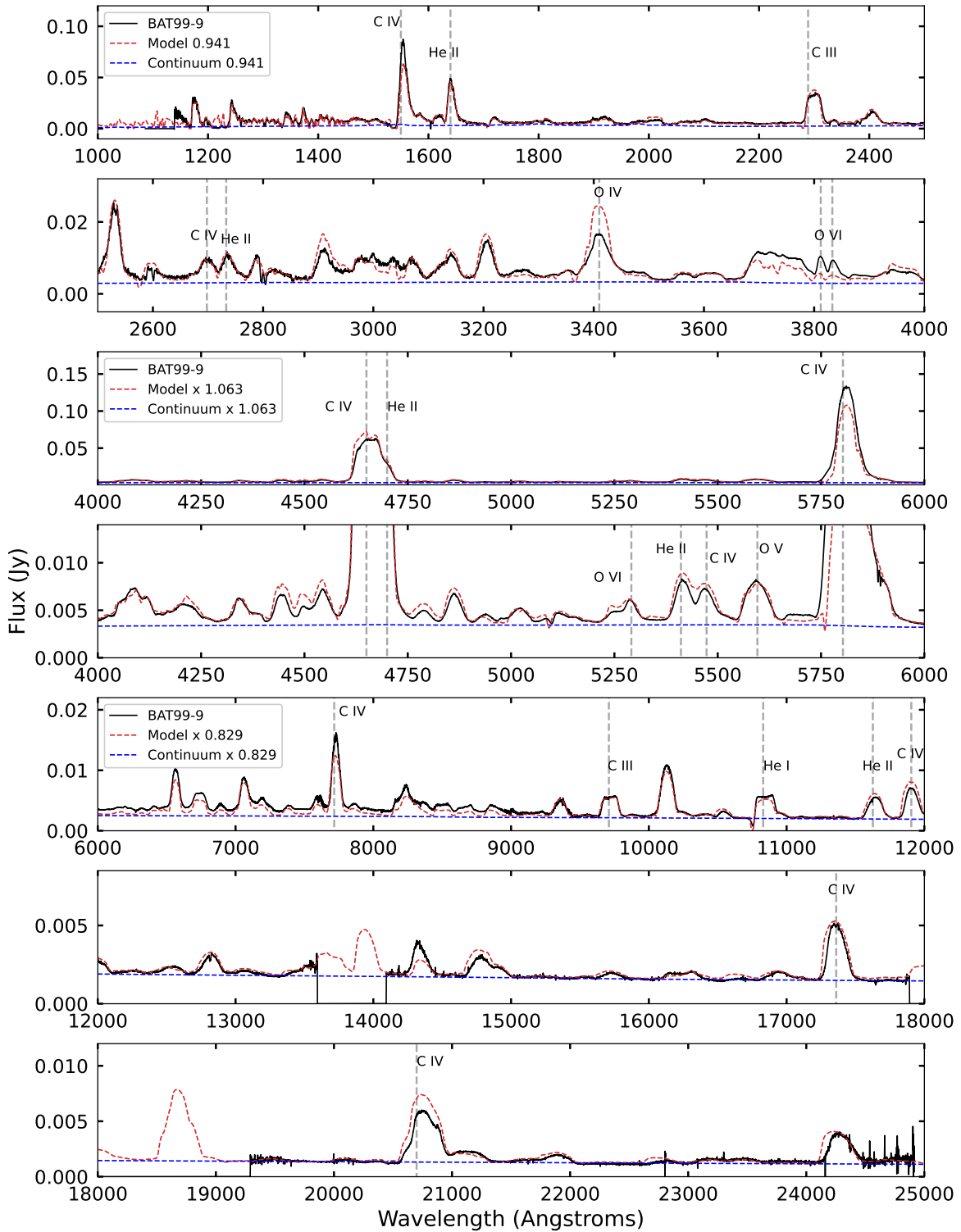


Figure 3. The observed spectrum of BAT99-9 (black) with the best fit model (red dashed) and the model's continuum (blue dashed). The model was scaled to the spectrum's continuum. The labeled emission lines are those primarily used for modeling the spectrum. The model's physical parameters are compromised to get the best fit model; therefore, there are some features in the spectrum that are not fit as well as others.

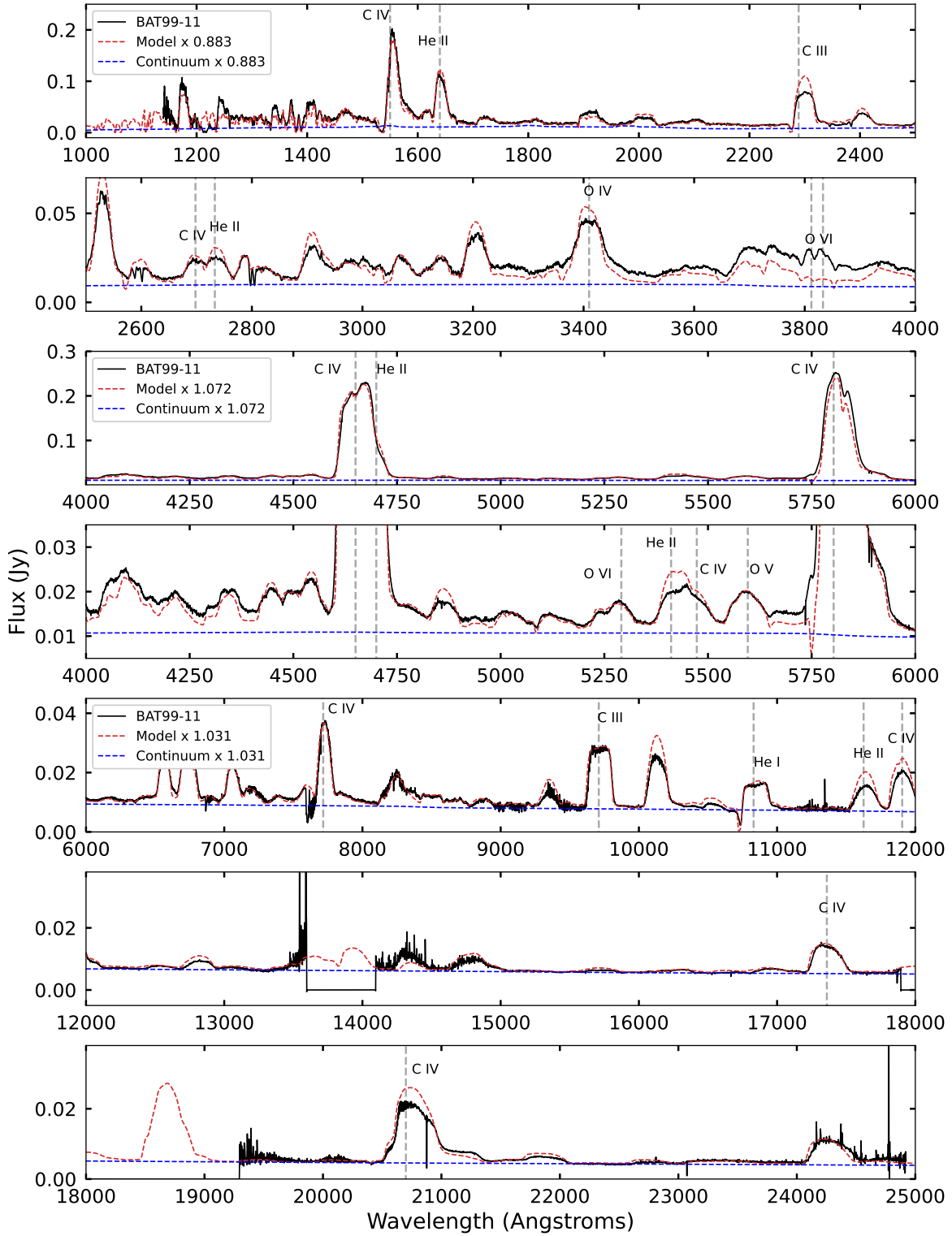


Figure 4. The observed spectrum of BAT99-11 (black) with the best fit model (red dashed) and the model's continuum (blue dashed). The model was scaled to the spectrum's continuum. The labeled emission lines are those primarily used for modeling the spectrum. The model's physical parameters are compromised to get the best fit model; therefore, there are some features in the spectrum that are not fit as well as others.

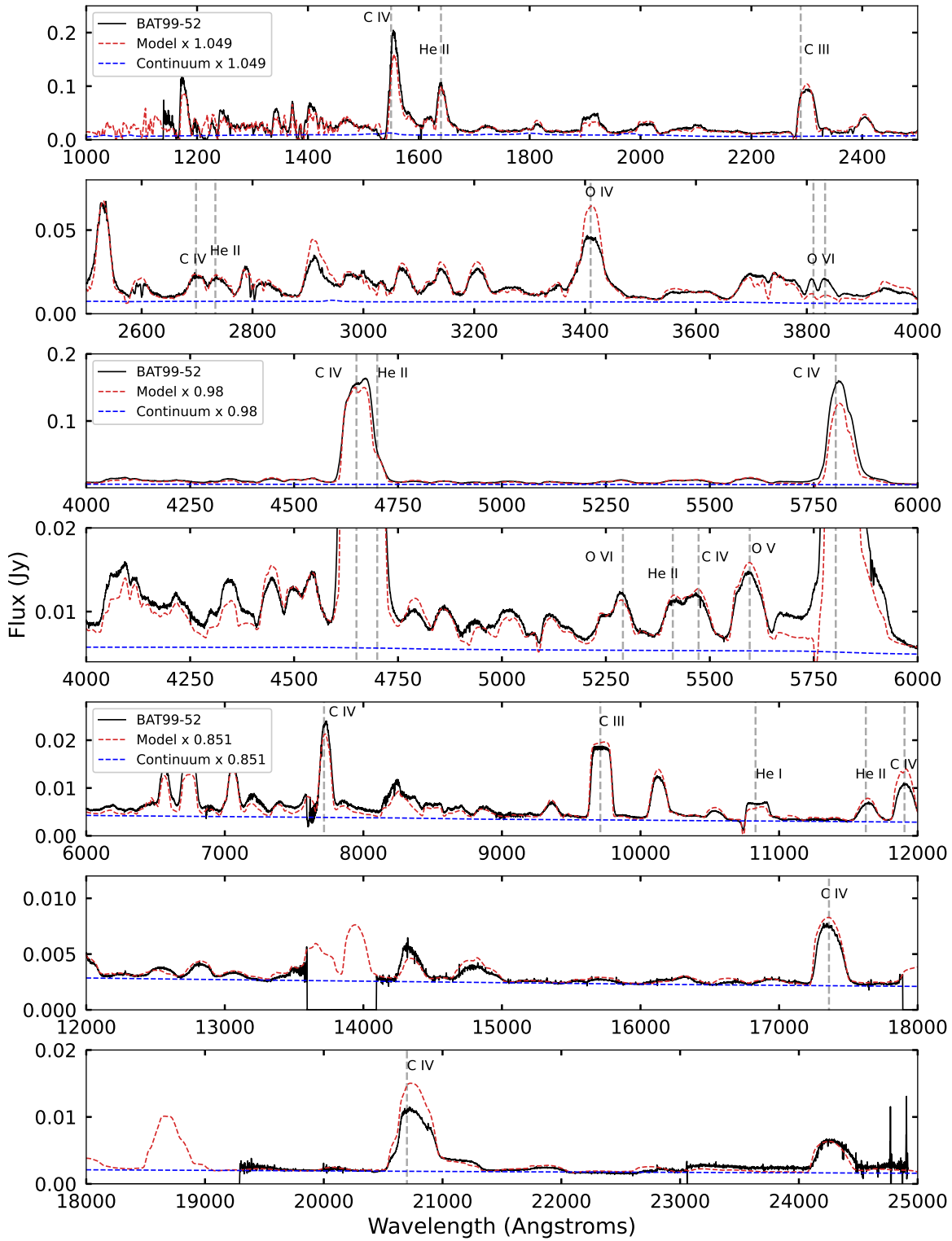


Figure 5. The observed spectrum of BAT99-52 (black) with the best fit model (red dashed) and the model's continuum (blue dashed). The model was scaled to the spectrum's continuum. The labeled emission lines are those primarily used for modeling the spectrum. The model's physical parameters are compromised to get the best fit model; therefore, there are some features in the spectrum that are not fit as well as others.

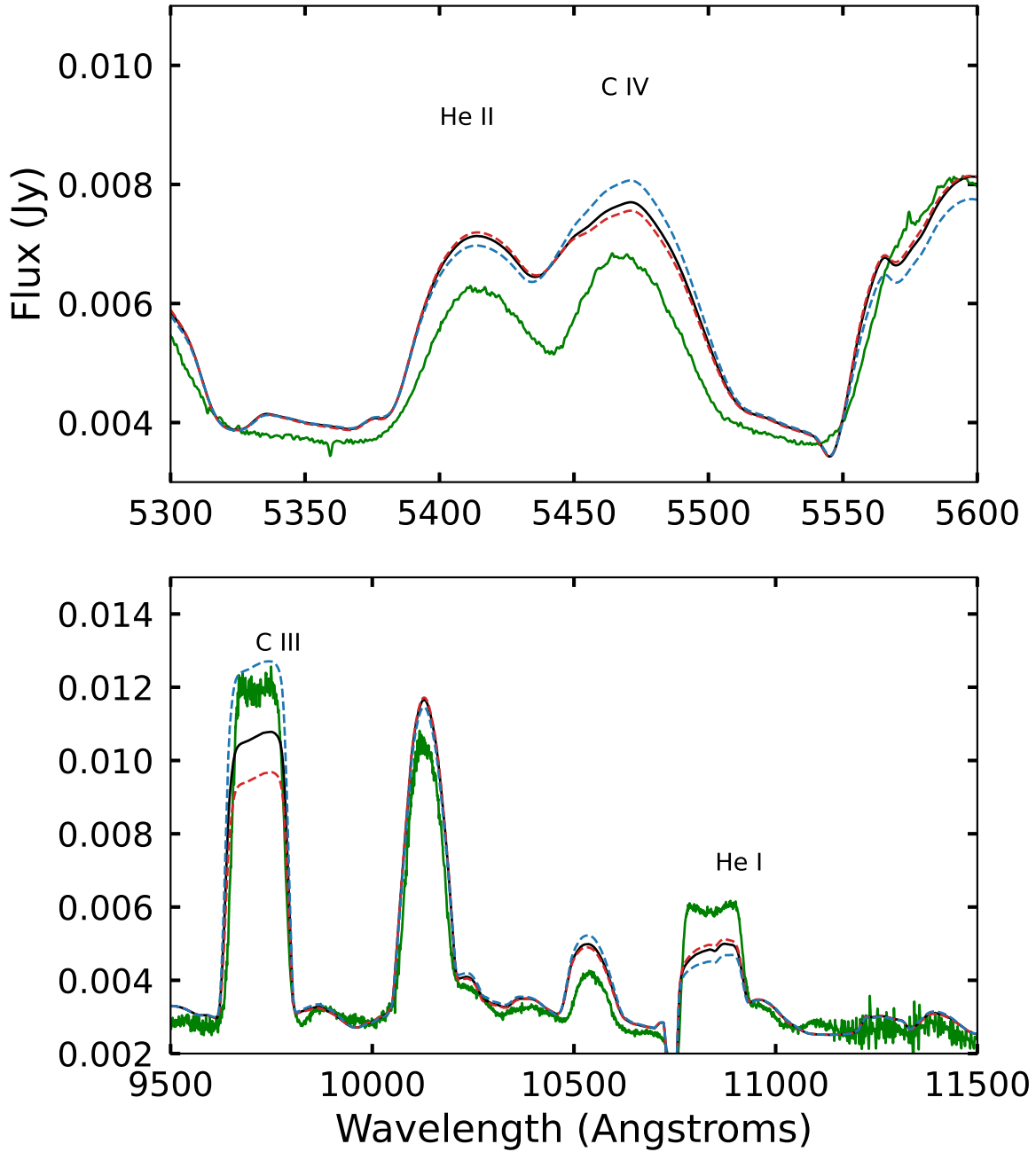


Figure 6. C/He uncertainty models. The carbon/helium line pairs, C IV $\lambda 5473$ /He II $\lambda 5411$ and C III $\lambda 9710$ /He I $\lambda 10830$, used to determine the uncertainty of the model's C/He abundance. BAT99-8's spectrum (green) and its' best model ($X(C)/X(He) = 0.83$, black) with the lower uncertainty limit ($X(C)/X(He) = 0.75$, red dashed) and upper uncertainty limit ($X(C)/X(He) = 1.08$, blue dashed) scaled by 0.927 for the top plot and 1.085 for the bottom plot. The lower C/He uncertainty was stopped before the C IV $\lambda 5473$ and He II $\lambda 5411$ lines flipped flux strengths or had the same flux strength as that would not be representative of the star. This resulted in the lower C/He limit being very similar to the best model abundances. However, both the upper and lower C/He uncertainty at the C III $\lambda 9710$ and He I $\lambda 10830$ lines do not represent the correct ratio, whereas the best model is equally too low for both the C III and He I lines giving a ratio that is representative of the star.

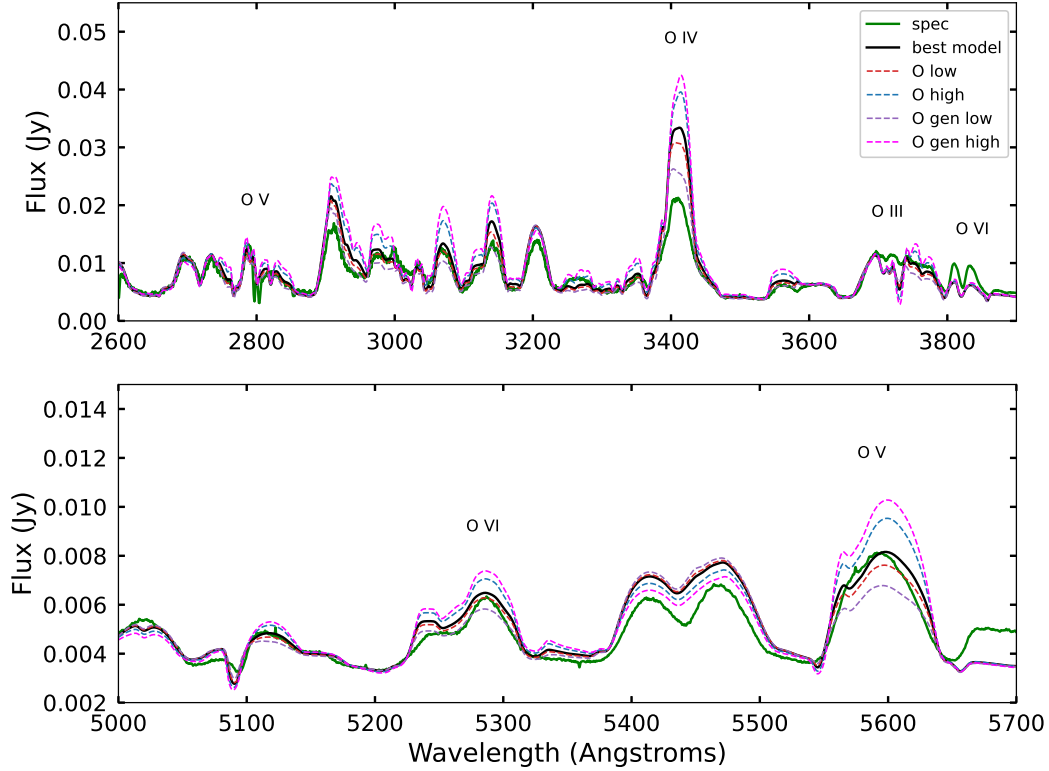


Figure 7. Oxygen uncertainty models. BAT99-8 (green) with its best model ($X(O) = 0.077$, black) and the “generous” and realistic oxygen abundance uncertainty models scaled by 0.927 in the top plot and by 0.930 in the bottom to match the spectrum’s “continuum.” The realistic uncertainty models (lower: $X(O) = 0.06$, red; upper: $X(O) = 0.14$, blue) were adopted as the uncertainties on the oxygen abundance. The “generous” uncertainty models (lower: $X(O) = 0.04$, purple; upper: $X(O) = 0.21$, magenta) were used to show the limits of the oxygen abundance in the star. The realistic uncertainties were determined primarily using the O VI $\lambda 5291$ (recombination line) and O V $\lambda 5596$ lines. The O IV $\lambda 3400$ line was used to determine the lower “generous” oxygen abundance as when we get close to fitting the $\lambda 3400$ line, the other model oxygen lines become too low to fit the spectrum. The upper “generous” limit was found by making all of the model oxygen lines too high for the spectrum. The O IV $\lambda\lambda 3811, 3834$ doublet is not reproduced well in the spectrum (see Appendix D).

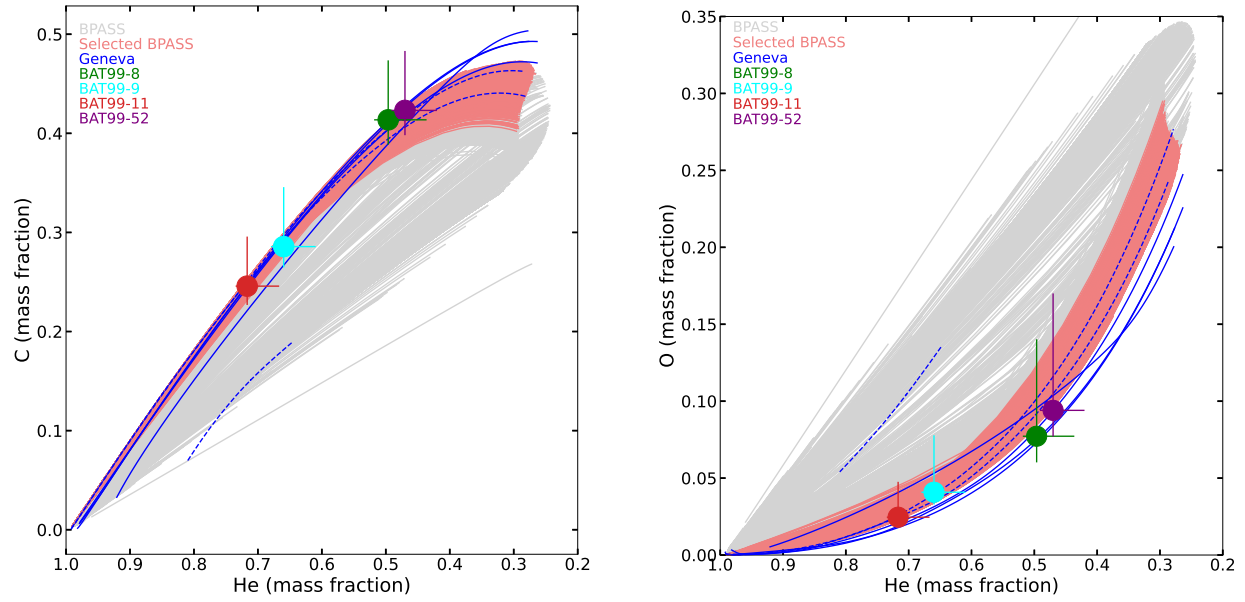


Figure 8. Helium vs. Carbon and Oxygen mass fractions. The BPASS models (gray; coral for models with similar chemical abundance ratios as the WC-type stars), Geneva solar models (solid blue), and Geneva LMC models (dashed blue) show the evolutionary tracks of the models containing a WC phase. The 4 WC stars are represented as the dots (BAT99-8: green, BAT99-9: cyan, BAT99-11: red, and BAT99-52: purple). The mass fractions for He, C, and O of the four WC stars are in agreement with both the Geneva single-star and BPASS binary evolutionary models. In fact, the stars follow the evolutionary tracks, e.g. BAT99-9 and BAT99-11 appear to be less chemically evolved than BAT99-8 and BAT99-52 (have a higher C and O abundance).

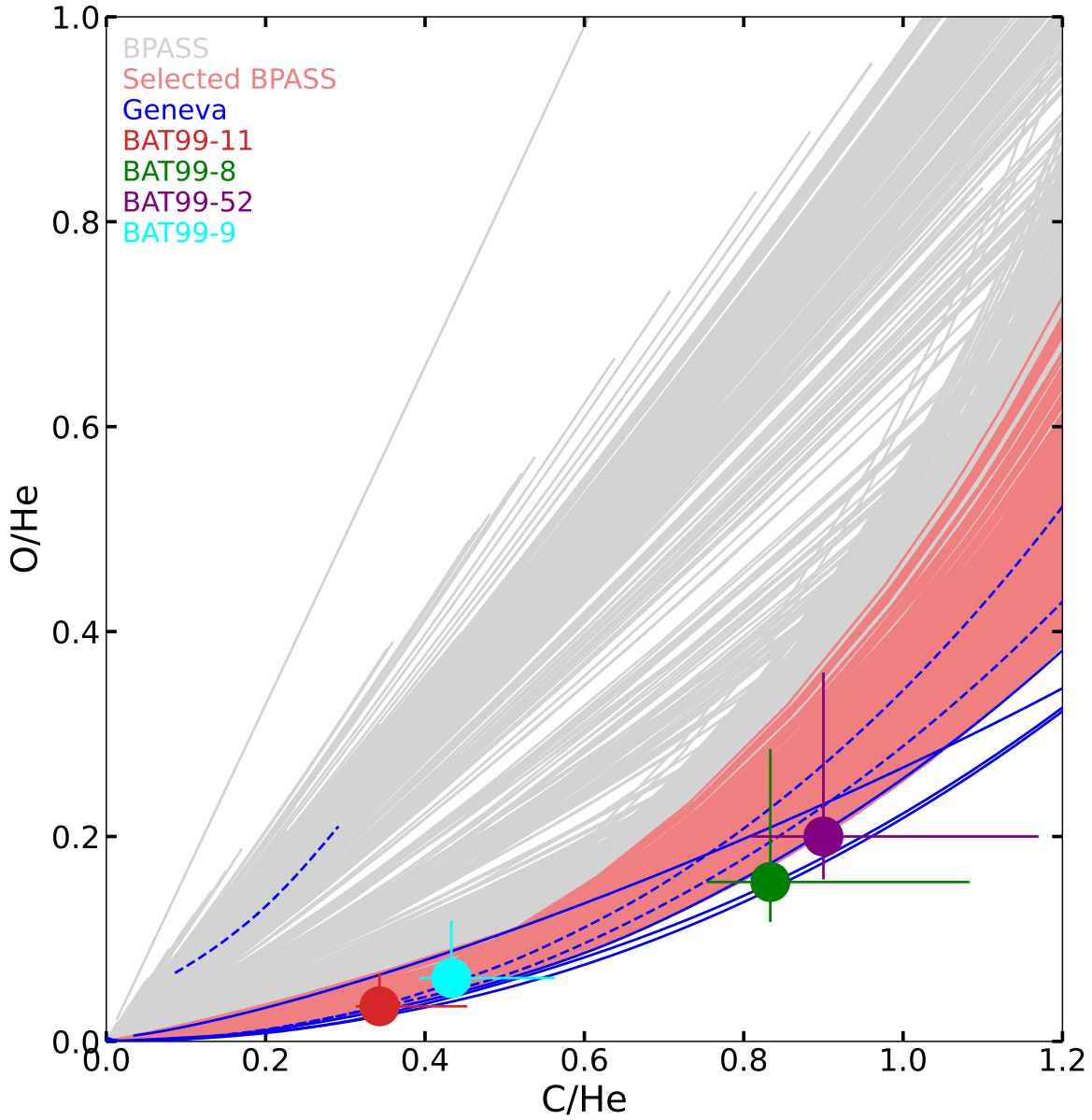


Figure 9. O/He vs. C/He plot. BAT99-8 (green), BAT99-9 (cyan), BAT99-11 (red), and BAT99-52 (purple) are shown as dots on the plot. The BPASS (gray), Geneva LMC (dashed blue), and Geneva solar metallicity (solid blue) models show the evolutionary tracks for the WC phase. The 4 WC stars lie directly on the Geneva solar metallicity models, specifically the 60, 85, and 120 M_{\odot} progenitor solar metallicity models. The 40 M_{\odot} progenitor solar and 85 and 120 M_{\odot} progenitor LMC metallicity models are in the region but have higher O/He values. The Geneva model with a much higher O/He than the stars for a given C/He value is the 60 M_{\odot} progenitor LMC metallicity model. The BPASS models span a larger range of O/He values, so only about a third of their models (coral) are near the WC-type stars.

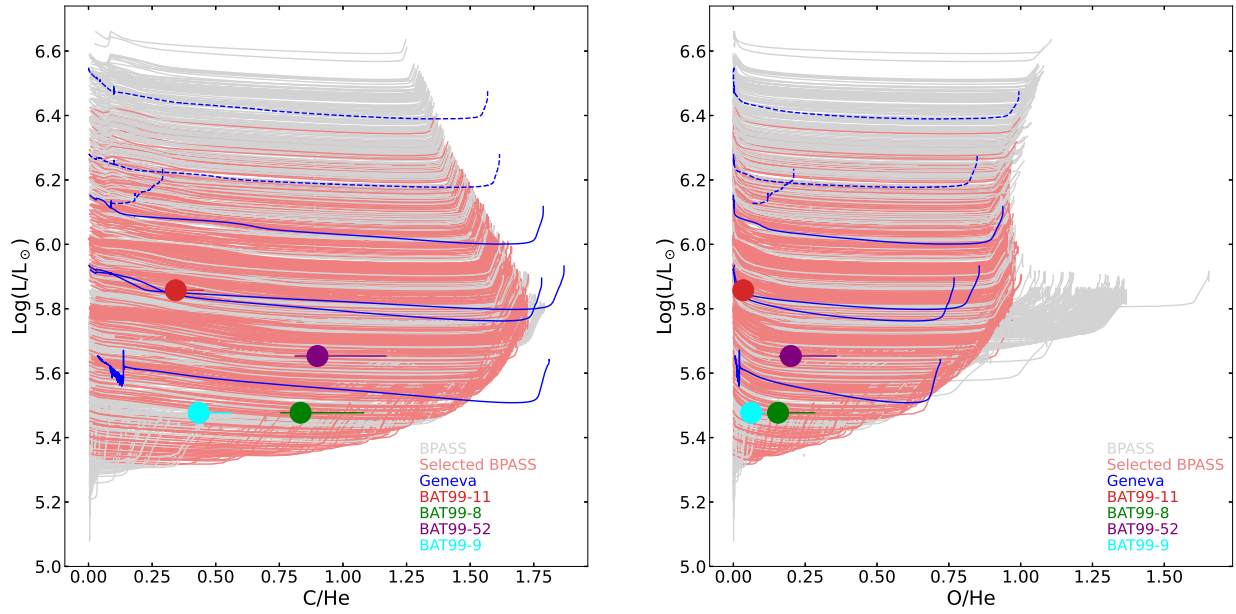


Figure 10. Luminosity vs. chemical abundance mass ratios C/He and O/He. The BPASS models (gray), Geneva solar models (solid blue), and Geneva LMC models (dashed blue) show the evolutionary tracks of the models containing a WC phase. The 4 WC stars are represented as the dots (BAT99-8: green, BAT99-9: cyan, BAT99-11: red, and BAT99-52: purple). While the Geneva LMC metallicity single-star models do not intercept with the WC stars, the BPASS binary and Geneva solar metallicity models do. The progenitor mass $40M_{\odot}$ Geneva single-star model is the model closest to BAT99-8 and BAT99-9. The BPASS models that were near the WC-type stars in Figure 9 are displayed in coral.

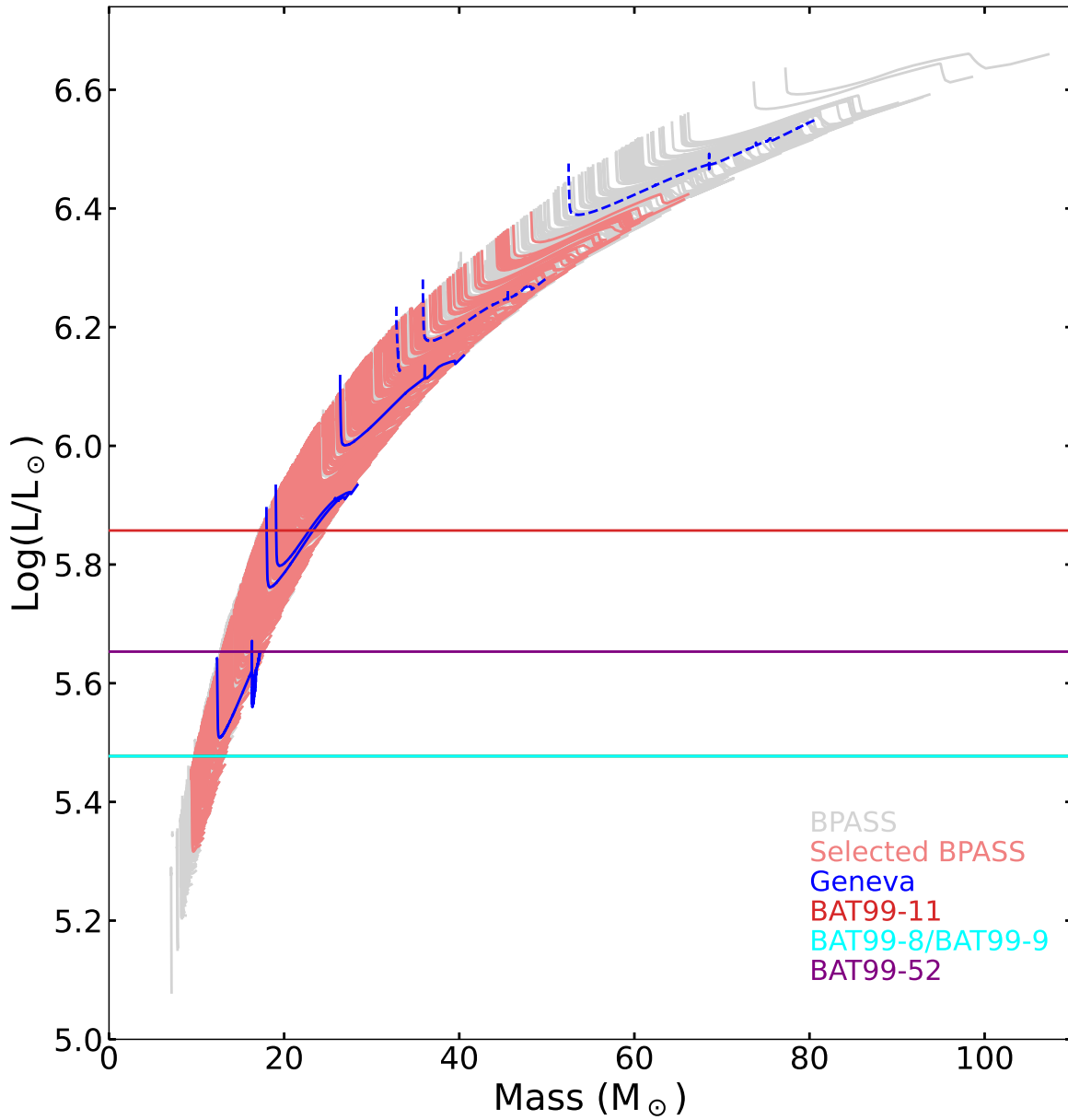


Figure 11. Luminosity vs. WC mass. The 4 WC stars are indicated by lines across the plot (BAT99-8/BAT99-9: cyan, BAT99-11: red, and BAT99-52: purple). BAT99-8 and BAT99-9 have the same luminosity so are represented by one line. The BPASS models (gray; models near WC-type stars in Figure 9 are coral) and Geneva models (Geneva metallicity: blue solid; LMC metallicity: blue dashed) have the same luminosity-mass relation, indicating that the type of evolution might not matter for WC-type stars.

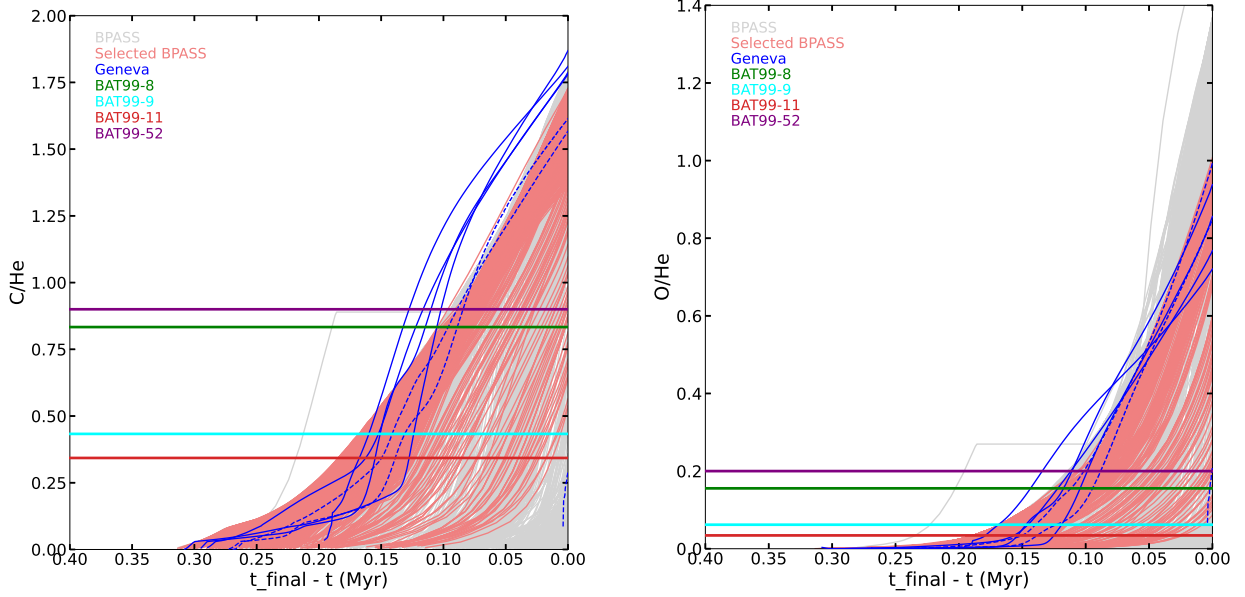


Figure 12. Chemical abundance mass ratios, C/He and O/He, vs. time before the star goes supernova. BPASS (gray), BPASS selected for being near the WC-type stars in Fig 9(coral), Geneva solar (solid blue), and Geneva LMC (dashed blue) models of the WC phase are compared to the WC stars which are represented as horizontal lines since their age is unknown (BAT99-8: green, BAT99-9: cyan, BAT99-11: red, and BAT99-52: purple). The times at which the stars' C/He and O/He overlap the evolutionary models occurs within a few hundredths of a Myr from each other.

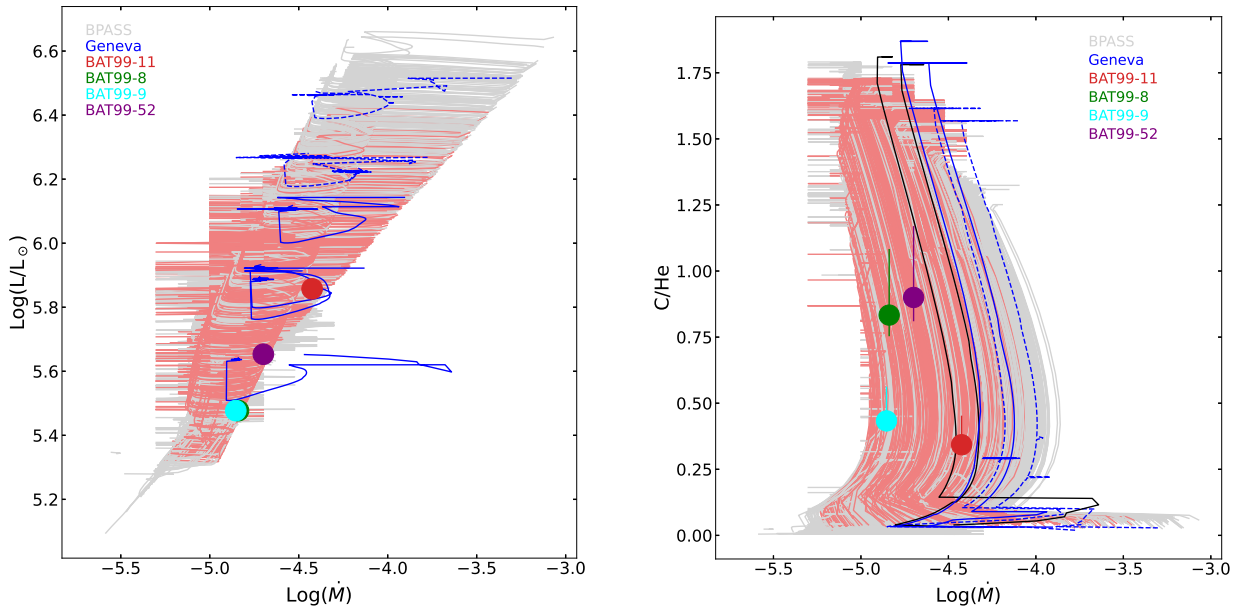


Figure 13. Luminosity and Chemical abundance ratio, C/He, vs. Mass-Loss Rate. BPASS (gray), BPASS selected for being near the WC-type stars in Fig 9(coral), Geneva solar (solid blue), and Geneva LMC (dashed blue) models of the WC phase are compared to the four WC stars represented as dots (BAT99-8: green, BAT99-9: cyan, BAT99-11: red, and BAT99-52: purple). The stars agree with the Geneva solar metallicity models and the BPASS models.

APPENDIX

Systematic errors are a major concern in modeling stellar atmospheres. They occur because of inaccuracies in the modeling, because of assumptions used in the modeling, and because of biases of those doing the analyses. Below we address four concerns:

1. The insensitivity of the model to the adopted stellar radius.
2. Hydrodynamics and radiative driving.
3. Clumping.
4. The inability to fit O VI $\lambda\lambda 3811, 3834$.

A. THE INSENSITIVITY OF THE MODEL TO THE ADOPTED STELLAR RADIUS

The winds of WC stars are optically thick, and as a consequence the radius of the hydrostatic core is not well constrained by spectral modeling (e.g., Hillier 1991a; Najarro et al. 1997; Hamann & Gräfener 2004) – its determination requires detailed hydrodynamic modeling that is beyond the scope of the current paper.

The difficulties in calculating the hydrodynamic structure are manifold. In particular, calculations show that the iron opacity bump is crucial for driving the winds in early-type WN stars and WC stars (e.g., Nugis & Lamers 2002; Grassitelli et al. 2018; Gräfener & Hamann 2005; Sander et al. 2020). This opacity can push the star above the effective Eddington limit⁵ which can trigger weak convection, density inversions, a wind to be launched, or cause the radius of the star to inflate (Ishii et al. 1999; Gräfener et al. 2012). A further complication is that there are instabilities in a medium when it is close to the Eddington limit (e.g., Shaviv 2001). Handling such structures will require time-dependent 3D radiation hydrodynamics. Since we cannot derive a stellar radius, we cannot determine effective temperatures for comparison with stellar evolution calculations (which also suffer from the aforementioned difficulties).

Surprisingly, the determination of the stellar luminosity appears to be much more robust – the luminosity is one of the principal factors controlling the ionization structure of the wind, and hence the relative strength of lines belonging to a single chemical element but in different ionization states (e.g., C II, C III, C IV). We do stress, however, that the flux we can observe (ie., that longward of the Lyman edge at 912 Å) constitutes only $\sim 30\%$ of the emitted energy for the stars studied in this paper.

B. WIND HYDRODYNAMICS AND RADIATIVE DRIVING.

Ideally we would like to compute the structure of the wind from first principles. Such calculations are presently intractable, but can be done in more limited forms. For example, the clumping structure (see below) can be specified (Gräfener & Hamann 2005; Sander et al. 2020). It is also very difficult to get the calculations to give the same qualitative agreement with observations as in models where the velocity law and mass-loss rate are treated as free-parameters, although the self-consistent model of Gräfener & Hamann (2005) does come close. As noted by Gräfener & Hamann (2005), the hydrodynamic solutions are also very time consuming.

As for O stars, CMFGEN allows a consistency check between radiative force obtained in the modeling and that required to drive the wind. Since we cannot determine the stellar gravity, the gravity and mass are free parameters. However, stellar evolution predicts a relatively tight relation between mass and luminosity for He-burning WR stars (Langer 1989). Unfortunately there is scatter. In the BPASS models the range is of order $\pm 10\%$ for masses less than $20 M_{\odot}$, and somewhat larger for higher masses. While such a range is small, it could have a crucial influence when the star is very close to the Eddington limit.

In most of our modeling we adopted a smaller set of species and ionization stages than warranted by the density and temperature structure of the atmosphere. With this data set there is a large inconsistency between the radiative force

⁵ Defined using all opacity sources, not just that due to electron scattering which is used to define the classical Eddington limit.

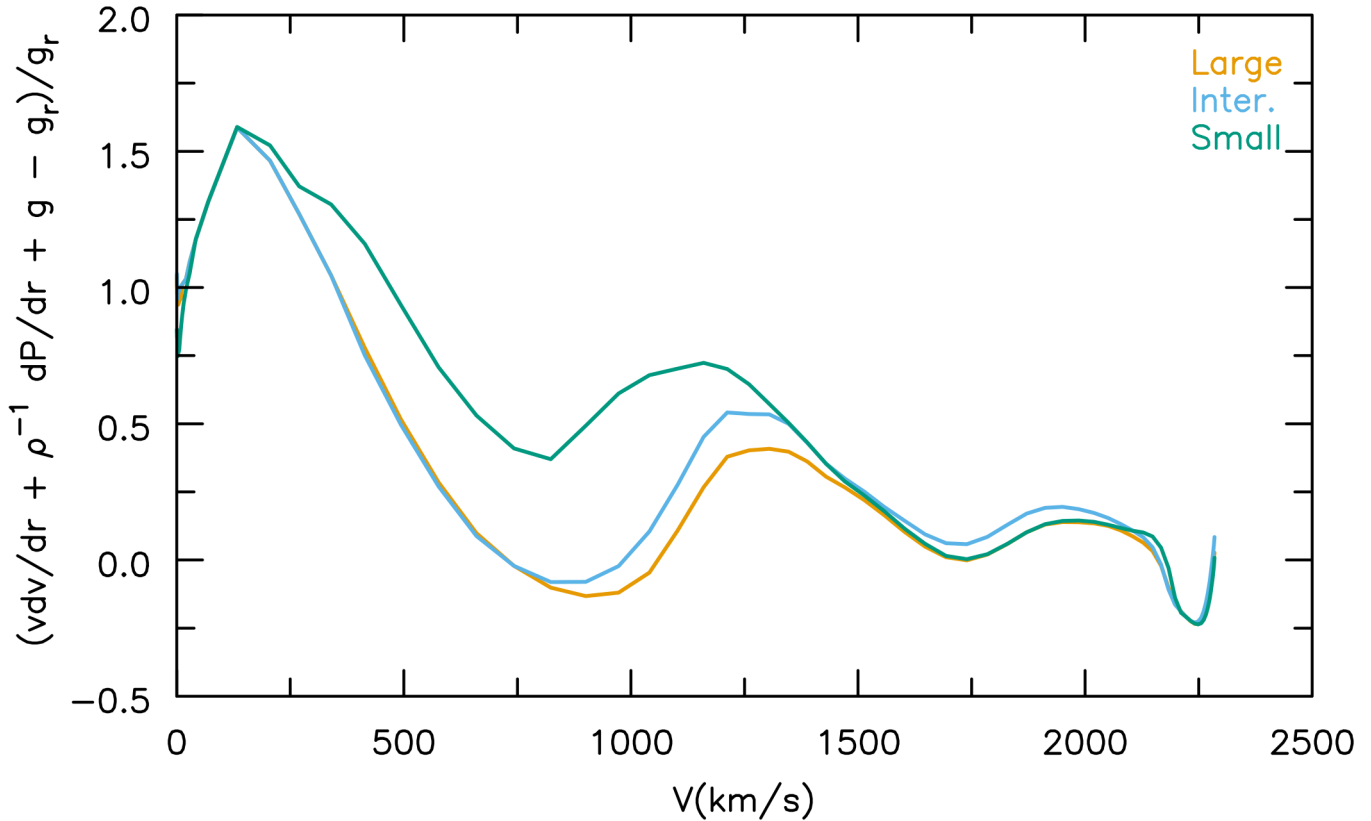


Figure 14. Check on the consistency of the radiative force needed to drive the mass-loss for the assumed clumping and velocity law. The most significant discrepancy occurs below 500 km s^{-1} . The small case refers to the atomic data used to compute the models used in this study (4297 levels, 123 ionization states, 373 238 lines); the intermediate case uses ionization stages and levels (5290 levels, 130 ionization states, 844, 731 lines), while the largest set had 6209 levels, 20 chemical species, 149 ionization states, and treated 1 210 981 lines. All models had 18 or 19 chemical species: H, He, C, O, N, Ne, Na, Mg, Al, Si, P, S, Cl, Ar, Ca, Cr, Mn, Fe, and Ni.

obtained in the modeling and that required to drive the wind. Considerable improvement was obtained by choosing more species, and more ionization stages, and by making other improvements in some of the atomic data (e.g., by including intercombination transitions) although in general there are still regions where the radiative force lies below that required to drive the flow. A summary of the model ions, the number of super levels, and number of full levels for the small data set is provided in Table 3. In Table 4 we provide a list of changes in the atomic models between the “small” and “intermediate” atomic models. Additional species that were included in the “large” model are listed in Table 5. Ni IX was also included in this table since additional levels were used.

While the revised atomic model has a strong influence on the radiative force (Fig. 14), it has only a minor influence on the predicted spectrum. In the optical (λ 3000 to 10000 Å) the average flux (computed in pixel space without regard to resolution) differed by less than 3%, and the statistical variation between the spectra was less than 4% (1 sigma). The most significant changes occurred for the O V $\lambda\lambda$ 5571 – 5607 / O III λ 5592 blend, and C III $\lambda\lambda$ 9701 – 9719 which were enhanced by roughly 20% in model computed with the revised atomic model. Similarly in the UV changes, except in some deep P Cygni absorptions, were less than 10%, and the statistical variation was less than 5%. The models used have a luminosity of $3 \times 10^5 L_{\odot}$ and a stellar mass of $15.0 M_{\odot}$ (the mass derived from the formula of Langer 1989 is $14.8 M_{\odot}$).

In order to drive a stellar wind it is necessary that the radiative force increases as we pass through the sonic point⁶. Because of the Fe-opacity bump, this can place limits on the temperature and density structure at the sonic point (e.g., Nugis & Lamers 2002; Gräfener & Hamann 2005). Indeed, by adjusting the radius of our models we can improve the consistency in the hydrodynamics around the sonic point. Again, this does not lead to significant spectral changes, and hence does not lead to significant changes in the stellar luminosity, or abundances.

Because the inner wind is optically thick we have no direct constraints on the velocity law in a large portion of the wind. However, in principle, we can constrain $V(r)$ in the outer wind through profile fitting. Unfortunately even this is difficult because of severe blending, and because the profiles also depend on the variation of the clumping factor with radius.

Sander et al. (2020) derived self-consistent mass loss rates for galactic WC stars from hydrodynamic models assuming a volume filling factor of 0.02 (set to 1 in the inner region). For a $\log(L/L_\odot)/(M/M_\odot)$ ratio of 4.3 (corresponding to $L = 3 \times 10^5 L_\odot$, $M = 15 M_\odot$) a mass-loss rate of $7 \times 10^{-6} M_\odot \text{ yr}^{-1}$ was derived. This is roughly a factor of 2 lower than our derived mass-loss rates for BAT99-8 and BAT99-9, but the discrepancy would be even larger if we allowed for the lower metallicity of our WC LMC stars.

C. CLUMPING

It is well known that the winds of WR stars (and O stars) are clumped. The strongest evidence for clumping in WR stars comes from variability studies (e.g., Moffat et al. 1988; McCandliss 1988; Lépine & Moffat 1999), and the weakness of the red-shifted electron-scattering wing relative to its associated emission line (e.g., Hillier 1991b). In WR stars the wings are redshifted because the typical expansion velocities ($\sim 2000 \text{ km s}^{-1}$) are much larger than the thermal motions of the electrons ($\sim 400(T/10^4)^{0.5} \text{ K}$). If we ignore the thermal motions, every scattering of a photon by an electron in a monotonic flow leads to a decrease in the photon’s energy. A major advantage of clumping is that it reduces the mass-loss rate, and hence it makes it easier for radiation pressure to drive the flow.

In CMFGEN we assume the clumping at a given radius to be uniform, and typically use two parameters to describe the radial variation of clumping – an onset velocity and the clumping at infinity. This prescription is completely ad hoc, and is not based on physics. We have very little idea of how the clumping varies with radius/velocity, and it is very difficult to derive constraints using observations. We also make a simplistic assumption to solve the radiative transfer equation. In particular we assume that the clumps are much smaller than a photon mean-free path, and that the interclump medium is void. Despite these assumptions and approximations, CMFGEN (and similar codes) are capable of producing theoretical spectra in excellent agreement with observations.

The choice of clumping law can have an influence on the quality of fits. As WR winds are optically thick, both the continuum (especially at optical and longer wavelengths) and lines originate in the wind. Since a strong emission line arises at larger radii than its adjacent continuum, its equivalent width will be affected by radial variations in clumping. Further, the biases introduced by our simplistic approach to clumping will influence line and continuum formation differently.

The influence of clumping is shown in Figs. 15 and 16 for three values of the volume-filling factor: 0.05 (used in this paper), 0.1, and 0.2. Because of blending and the absence of “line-free” regions, the influence of electrons is not as easily discerned as in WN stars. While a value of 0.2 can be ruled out by a comparison between model and observations, it is extremely difficult to place a lower limit on the clumping factor in WC stars. The redshift of the C IV $\lambda\lambda 1548, 1552$ transition, which is influenced by its large optical depth and the need to use a Voigt profile when computing the observed spectrum (Hillier 1989), also favors a volume-filling factor less than 0.2.

Because of the complexity of WC spectral formation, identical spectra are not obtained when \dot{M}/\sqrt{f} is held constant. However, generally only minor adjustments of one or more parameters (e.g., \dot{M} or L) are needed to obtain better agreement between models computed with different filling factors.

D. THE INABILITY TO FIT O IV $\lambda\lambda 3405 - 3414$ AND O VI $\lambda\lambda 3811, 3834$

As readily apparent from the modeling, there are a few significant discrepancies between the models and observations. There are many possible reasons for the discrepancies, and tracking down the source of a particular discrepancy is

⁶ At the sonic point the wind speed matches the isothermal sound speed. In thermal winds it is also a critical point of the flow – physically this occurs because material above the sonic point cannot communicate to material below the sonic point by sound waves. In radiative flows, in which the driving force depends on the velocity gradient, there is still debate about whether the critical point occurs at the sonic point, or at higher velocities (e.g., Lucy 2007). The latter is the case when the force has an explicit dependence on dv/dr as in the Sobolev approximation (e.g., Castor et al. 1975; Pauldrach et al. 1986).

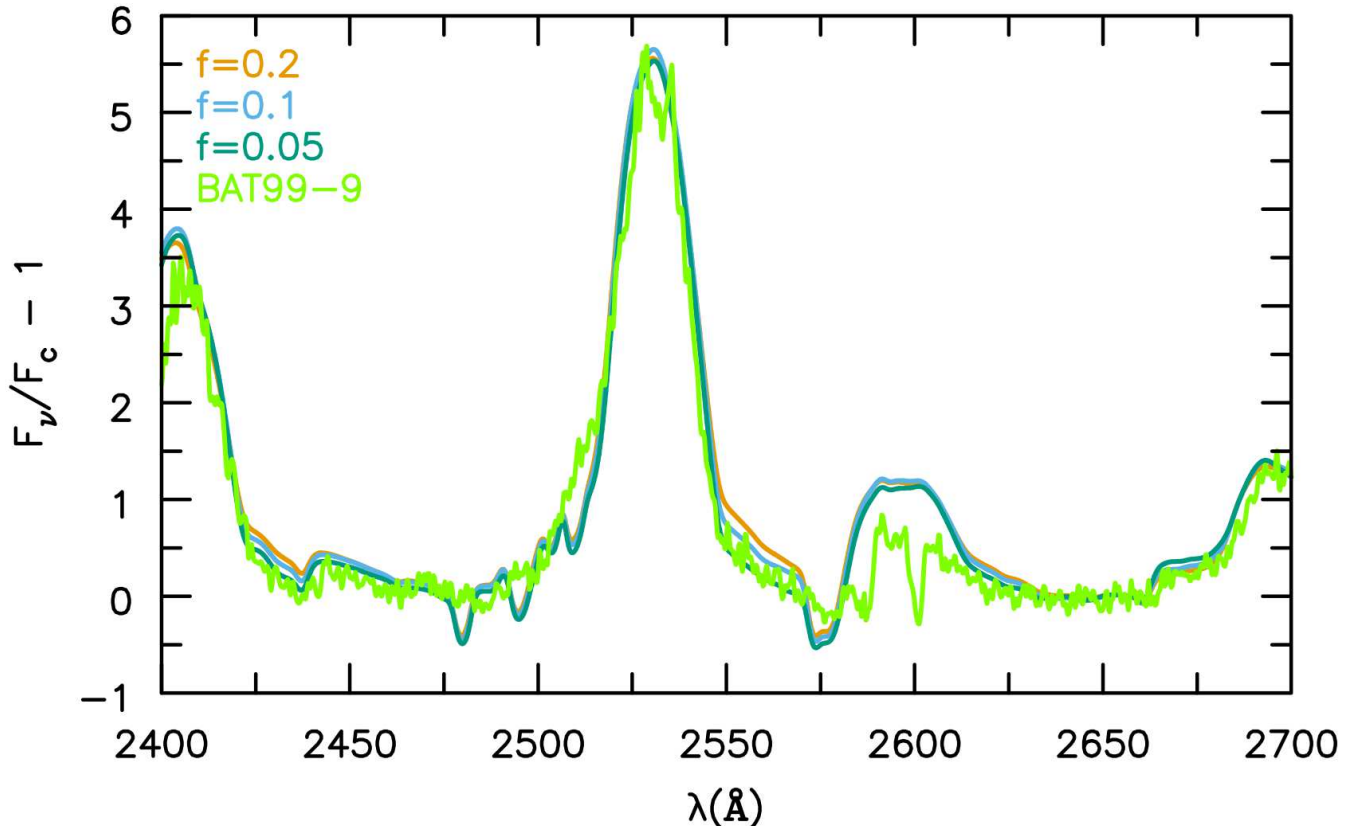


Figure 15. Illustration of the influence of different clumping factors on the C IV $\lambda 2530$ profile. To remove slight differences in the observed emission line strength relative to the model we scaled the continuum (seen at 2650 \AA) to unity, subtracted unity, and then scaled the observations so that the emission peak was in rough agreement. As apparent from the plot, a clumping factor of 0.2 leads to an electron scattering wing (between 2550 and 2575 \AA) that is too strong compared with the observations.

very difficult. With the current modeling two promising sources for the discrepancies are the adopted atomic models, and our simplistic treatment of radiative transfer in the clumped wind.

While a close examination of Figs 2-5 reveals many (minor) discrepancies many of these can be regarded as insignificant in the sense that that are likely to be due to issues with the adopted atomic data, or can be removed with a relatively minor change in the adopted stellar parameters. However, there are two major discrepancies between our theoretical spectra and observed spectra which are not easily explained. In particular, the strength of O IV $\lambda\lambda 3405 - 3414$ is consistently overestimated (factor of 2) while the O VI $\lambda\lambda 3811, 3834$ is underestimated (factor of 2 to 4). The latter problem has been seen in earlier modeling of WC stars (e.g., Hillier & Miller 1999; Crowther et al. 2002; Sander et al. 2012), and is also often seen when modeling WO stars (e.g., Tramper et al. 2015). Coincidentally, it is often seen for N V $\lambda\lambda 4604, 4620$ in WNE stars (O VI and N V are isoelectronic) (Hainich et al. 2014). However, it is unclear if the discrepancies have the same cause.

Despite many tests, we were unable to fit O VI $\lambda\lambda 3811, 3834$ while maintaining the fit to other spectral lines. Following the work of Gräfener & Hamann (2005) we did find that a reduction of clumping in the O VI $\lambda\lambda 3811, 3834$ formation region increased its strength (i.e., the equivalent width) significantly. Unfortunately the reduction in clumping reduced the IR fluxes (and to a lesser extent those in the optical), and this enhanced the EW of IR lines so that they were no longer compatible with observation.

We do not believe a significant increase in luminosity, alone, would solve the problem. The luminosity we derive is constrained by lines due to multiple ionization stages – He I/He II, C III/C IV, and O III/O IV/O V/O VI. We did try enhancing the clumping in the C III/He I in the formation zone (i.e., by decreasing f by roughly a factor of 2) to compensate for the higher luminosity but none of the models were satisfactory.

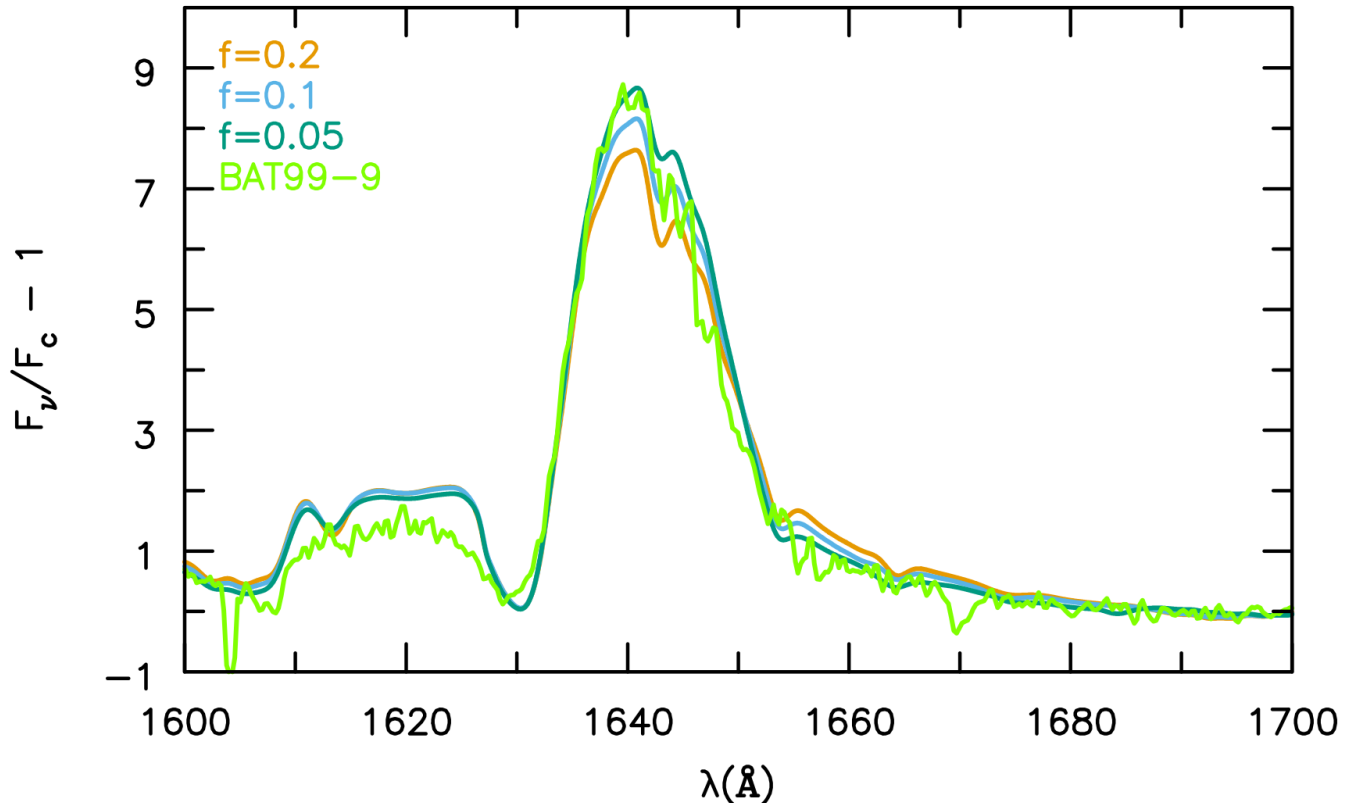


Figure 16. Similar to 15 but for He II $\lambda 1640$. The continua were scaled to match but no additional scaling was performed. Again we see that a clumping factor of 0.2 leads to an electron scattering wing (between 1650 and 1670 Å) that is too strong compared with the observations.

It may be possible to get a better fit to O VI $\lambda\lambda 3811, 3834$ by simultaneously increasing the luminosity and altering \dot{M} and the run of clumping with radius. By increasing the luminosity by 30%, it is possible to get the strength in close agreement with that observed. In the best model we had $f = 0.1$ in the inner wind decreasing to 0.5 in the outer wind – the later being necessary to get the lower ionization lines closer to that observed. However in this model O V $\lambda\lambda 5571 - 5607$ is now a factor of two stronger than observed, and most of the C IV are systematically too strong. It is possible that a more sophisticated treatment of clumping would solve the problem with O VI $\lambda\lambda 3811, 3834$. In our models there is no shortage of photons – the line simply has a very large optical depth which inhibits photon escape.

A crucial confirmation of our models is that the O VI recombination line ($n = 8$ to $n = 7$) at $\lambda 5290 \text{Å}$ (although blended) matches reasonably well. Fortunately this line in WO stars is clean, and this will greatly aid in constraining the oxygen abundance in WO stars.

Sander et al. (2012) were able to fit O VI $\lambda\lambda 3811, 3834$ in the galactic WO star WR102 using the PoWR code (Gräfener et al. 2002; Sander et al. 2015). The derived luminosity was $\log L/L_{\odot} = 5.68$ (for a DM= 12.39; $\log L/L_{\odot} = 5.58$ when corrected to the Gaia DR2 DM of 12.14, Sander et al. 2019), significantly higher than the value of $\log L/L_{\odot} = 5.45$ (5.0 for DM= 12.14) found by Tramper et al. (2015). The difference in the results is at least partially attributable to the fitting procedure. While Sander et al. (2012) fitted O VI $\lambda\lambda 3811, 3834$ the fit to lower ionization lines, such as O V $\lambda\lambda 5571 - 5607$ was very poor. Conversely, Tramper et al. (2015) failed to fit O VI $\lambda\lambda 3811, 3834$ but the fit to the lower ionization lines was much better⁷. In WO stars O VI $\lambda\lambda 3811, 3834$ is one of the strongest lines in the optical, while in WC 4 stars it is a minor feature.

As noted earlier we also fail to fit O IV $\lambda\lambda 3405 - 3414$, the $2s^2 3p^2 P^{\circ} - 2s^2 3d^2 D$ multiplet. The line is blended with the weaker $2s 2p(^3P^{\circ}) 3s^4 P^{\circ} - 2s 2p(^3P^{\circ}) 3p^4 D$ transition. Two other O IV multiplets, $2s^2 3s^2 S - 2s^2 3p^2 P^{\circ}$

⁷ For the two galactic stars analyzed by Sander et al. (2012) the He:C:O mass percentages were 30:40:30 while Tramper et al. (2015) obtained 14:62:24 for WR102 and 26:54:21 for WR142.

($\lambda\lambda 3063-3072$) and $2s\ 2p(^3P^\circ)\ 3p\ ^3P-2s\ 2p(^3P^\circ)\ 3d\ ^2F^\circ$ ($\lambda\lambda 3560-3593$) are in better agreement with the observations. An examination of the models and line rates found no obvious cause for the discrepancy.

E. ATOMIC DATA

To do the modeling presented in this paper a great deal of atomic data is needed. The data we used comes from a wide variety of sources and is of uneven quality. Tests with different atomic data sets generally did not yield significant spectral changes for lines used in the spectral fitting. This, by itself, does not prove the accuracy of the atomic data – different data sets can suffer from the same limitations. In the present work we include low temperature dielectronic recombination which typically arises from doubly excited states that lie just above the ionization limit. On the other hand we neglect high temperature dielectronic recombination (HTDR) that typically arises from doubly excited states with high n (~ 100). For example, in C III HTDR occurs via $2p\ nl$ transitions. The difficulty of treating HTDR is severalfold – it occurs from very large n (and low l) values and it can be suppressed at high densities (e.g., Burgess & Summers 1969; Kaur et al. 2018). Further, in WR stars the radiation can not be neglected, and this will also suppress HTDR.

Below we list the sources of atomic data used in the WC calculations. All data are available through the CMFGEN website www.pitt.edu/~hillier. When changes are made to the atomic species, a new sub-directory is created.

E.1. Energy levels

In general we used energy levels from NIST. For many species we used the atomic data of Bob Kurucz (Kurucz 2009) that is available through his website Kurucz (2010). An advantage of this data is that in most cases the data already contain NIST energies (when available), and does not assume LS coupling. For energies not available through NIST (or Kurucz) we typically used scaled theoretical energies, while hydrogenic values were adopted for high (n, l) states. To facilitate modeling large atoms, high l states were typically grouped into a single state (denoted by z), while high states (e.g. C IV nl , $n > 12$) were treated as a single level (denoted by w). This grouping is done during the creation of the model atom, and is distinct from the grouping of model atom levels into super levels.

E.2. Oscillator Strengths

The main sources of oscillator strengths are TOPbase (Cunto et al. 1993), which provides data computed by the Opacity Project (Seaton 1987), NORAD (Nahar 2010), and Kurucz (2010). For some species, oscillator strengths have been updated with oscillator strengths from NIST. Oscillator strengths for transitions from high (n, l) levels are scaled hydrogenic.

Many of the calculations (e.g., those in TOPbase) assume LS coupling, and often only include levels up to a principal quantum number (n) of 10. We performed fine structure splitting of the oscillator strengths assuming LS coupling, and used hydrogenic values for high l and n states.

E.3. Photoionization

The main sources of photoionization cross-sections are the Opacity Project (Seaton 1987; obtained from TOPbase Cunto et al. 1993), NORAD (Nahar 2010), and Kurucz (2010). Hydrogenic values were also used for the photoionization cross-sections from high l and n states. Recombination is treated using the same photoionization cross-sections.

E.4. Collisional data

For species/transitions without collisional data (or simply not yet implemented in the database) we used either the approximate formulae of van Regemorter (1962), or adopted collision strengths from a nearby isoelectronic species.

E.5. Species references

E.5.1. Carbon

C IV oscillator strengths are from Leibowitz (1972), photoionization data is from Peach et al. (1988) and Leibowitz (1972), and collision strengths are from Cochrane & McWhirter (1983). C III oscillator strengths, photoionization data, and dielectronic line data are from P. J. Storey (private communication). Collision rates among the lowest six terms are from Berrington et al. (1985). C II oscillator strengths and photoionization cross-sections are from Davey et al. (2000) (& P. J. Storey, private communication). NIST (Kramida et al. 2012, 2012-10-15) values are used, when available. Collision rates are from Tayal (2008).

E.5.2. *Nitrogen*

N V oscillator strengths for $n < 6$ are from [Liang & Badnell \(2011\)](#), photoionization data is from [Peach et al. \(1988\)](#), and collision strengths for N V for $n < 6$ are from [Liang & Badnell \(2011\)](#). N IV oscillator strengths and photoionization cross-sections were computed by [Tully et al. \(1990\)](#) as part of the Opacity Project ([Seaton 1987](#)). The identification of the $2s4s^3S$ and $2p3p^3S$ states have been switched (see [Allard et al. 1991](#)). Oscillator strengths for N IV forbidden (and semi-forbidden) lines are from [Nussbaumer & Storey \(1979a\)](#). N IV LTDR oscillator strengths are from [Nussbaumer & Storey \(1983, 1984\)](#).

N III oscillator strengths and photoionization cross-sections were computed as part of the Opacity Project ([Seaton 1987](#)) and were obtained from TOPbase ([Cunto et al. 1993](#)). Transition probabilities for intercombination lines are from [Nussbaumer & Storey \(1979b\)](#). These are in reasonable agreement with experimental values found in the study of [Träbert et al. \(1999\)](#). Collision strengths for transitions amongst the first 20 levels are from [Stafford et al. \(1994\)](#).

E.5.3. *Oxygen*

O VI oscillator strengths for $n < 6$ are from [Liang & Badnell \(2011\)](#), photoionization data is from [Peach et al. \(1988\)](#), and collision strengths for O VI for $n < 6$ are from [Liang & Badnell \(2011\)](#). Oscillator strengths and photoionization cross-sections for O V are from [Tully et al. \(1990\)](#) and were computed as part of the Opacity Project. Data from [Nussbaumer & Storey \(1979a\)](#) were also used. Collision rates for the six lowest terms of O V are from [Berrington et al. \(1985\)](#). O IV oscillator strengths were computed as part of the Opacity Project ([Seaton 1987](#)). Intercombination data ($^2P\text{-}^4P$) for O IV is from the compilation of [Mendoza \(1983\)](#). Photoionization data is from [Nahar \(1998\)](#) and was obtained through NORAD ([Nahar 2010](#)), and collision rates are from [Zhang et al. \(1994\)](#). O III oscillator strengths and photoionization data are from [Luo et al. \(1989\)](#). Collisional data for the four lowest terms in O III are from the compilation of [Mendoza \(1983\)](#).

E.6. *Isoelectronic sequences*

Lithium sequence (Ne VIII, Na IX, Mg X, Al XI): Oscillator strengths and photoionization cross-sections are from [Peach et al. \(1988\)](#).

Beryllium sequence (Ne VII, Na VIII, Mg IX, Al X): Oscillator strengths and photoionization cross-sections were computed by [Tully et al. \(1990\)](#) as part of the Opacity Project.

Boron sequence (Ne VI, Na VII, Mg VIII, Al IX, Si X): Oscillator strengths and photoionization cross-sections were computed by J. A. Fernley, A. Hibbert, AE Kingston and M. J. Seaton (unpublished) as part of the Opacity Project. Collisional data for the sequence is from [Zhang et al. \(1994\)](#).

Carbon sequence (Ne V, Na VI, Mg VII, Al VIII, Si IX, S XI): Oscillator strengths and photoionization cross-sections are from [Luo & Pradhan \(1989\)](#). Collisional data for the 4 lowest terms is from [Lennon & Burke \(1994\)](#).

Nitrogen sequence (Ne IV, Na V, Mg VI, Al VII, Si VIII, S X): Oscillator strengths and photoionization cross-sections were computed by V. M. Burke and D. J. Lennon (unpublished) for the Opacity Project, and were retrieved from TOPbase.

Oxygen sequence (Ne III, Na IV, Mg V, Al VI, Si VII, S IX): Oscillator strengths and photoionization cross-sections were computed as part of the Opacity Project by K. Butler and C. J. Zeippen (unpublished). Intercombination rates are from [Galavis et al. \(1997\)](#) and [Mendoza Mendoza \(1983\)](#). Collision rates are from [Mendoza \(1983\)](#).

Flourine sequence (Ne II, Na III, Mg IV, Al V, Si VI, S VIII): Oscillator strengths and photoionization cross-sections were computed by K. Butler and C. J. Zeippen (unpublished) as part the Opacity Project.

Neon sequence (Mg III, Al IV, Si V, S VII): Oscillator strengths were computed by K. Butler and C. J. Zeippen (unpublished) for Opacity Project .

Sodium sequence (Mg II, Al III, Si IV, S VI): Oscillator strengths and photoionization cross-sections were computed as part the Opacity Project. Collision strengths (for $n < 7$) are from [Liang et al. \(2009\)](#).

Ca VII oscillator strengths and photoionization cross-sections were computed by C. Mendoza, W. Eissner, M. Le Dourneuf, C. J. Zeippen (unpublished) for the Opacity Project.

Ca VI oscillator strengths and photoionization cross-sections were computed as part of the Opacity Project by [Nahar & Pradhan \(1993\)](#).

Ca IV oscillator strengths and photoionization cross-sections were computed by K. Butler, C. Mendoza and C. J. Zeippen (unpublished) as part of the Opacity Project.

E.6.1. *Fe*

Oscillator strengths and photoionization cross-sections for Fe XVI were computed by K. T. Taylor (unpublished) as part of the Opacity Project. Oscillator strengths and photoionization cross-sections for Fe XV are from [Butler et al. \(1993\)](#). Oscillator strengths and photoionization cross-sections for Fe XIV data are from the Opacity Project [C. Mendoza, W. Eissner, M. Le Dourneuf, C. J. Zeippen (unpublished)].

Oscillator strengths and photoionization cross-sections for Fe XI, Fe XII, and Fe XIII were computed by C. Mendoza (unpublished) as part of the Opacity Project. Collision strengths for Fe XIII are from [Aggarwal & Keenan \(2005\)](#) and those for Fe XI are from [Aggarwal & Keenan \(2003\)](#).

Oscillator strengths for Fe IV – Fe X were computed by Bob Kurucz ([Kurucz 2009, 2010](#)). Photoionization cross-sections were obtained from TOPbase ([Cunto et al. 1993](#)). Collision strengths for Fe VI are from [Chen & Pradhan \(1999\)](#) while Fe IV collisional data is from [Zhang & Pradhan \(1997\)](#).

For other elements (e.g., Cl, Cr, Ni) less atomic data are available. Typically we used oscillator strengths from Bob Kurucz ([Kurucz 2009, 2010](#)) and NIST. We typically adopted hydrogenic photoionization cross-sections, or used cross-sections from a nearby species in the same isoelectronic sequence. Admittedly these are crude approximations, but they do allow more realistic models to be constructed.

Table 3. Small Atomic Model

Species	N_S	N_F	Level name ^a
He I	27	39	n(14)
He II	13	30	n(30)
He III	1	1	
C II	9	16	2s ² 3d ² D
C III	100	243	2p 4d ¹ D ^o
C IV	59	64	30
C V	43	107	2s ² 30w ¹ W
C VI	1	1	
N III	34	71	2s ² 5g ² G
N IV	34	60	2s 4f ¹ F ^o
N V	45	67	n(30)
N VI	1	1	
O II	14	29	2s ² 2p ² (³ P)3p ⁴ S ^o
O III	85	267	2s ² 2p 8g ¹ F ^o
O IV	220	324	2p ² (³ P)10p ⁴ S ^o
O V	75	152	2s 7f ¹ F ^o
O VI	41	47	12z ² Z
O VII	1	1	
Ne II	42	242	2s ² 2p ⁴ (¹ D)4d ² S
Ne III	57	188	2s ² 2p ³ (² D ^o)5d ¹ S ^o
Ne IV	45	355	2s 2p ³ (⁵ S ^o)5s ⁶ S ^o
Ne V	37	166	2s ² 2p 5f ³ G
Ne VI	36	202	2s ² 10z ² Z
Ne VII	38	182	2s 10z ¹ Z
Ne VIII	24	49	10p ² P ^o
Ne IX	1	1	
Na II	21	35	2p ⁵ (² P _{1/2})6s [2] _{1/2} ^o
Na III	25	144	2p ⁴ (³ P)6f ² D ^o
Na IV	34	154	2p ³ (⁴ S ^o)6f ⁵ F
Na V	39	245	2s ² 2p ² (³ P)7s ² P
Na VI	45	237	2s ² 2p 6d ¹ P ^o
Na VII	30	143	2s ² 6f ² F ^o
Na VIII	72	214	2p 7d ³ D ^o
Na IX	27	71	30w ² W
Na X	1	1	

Table 3 continued on next page

Table 3 (continued)

Species	N_S	N_F	Level name ^a
Mg III	29	201	$2p^5 10f^3 F$
Mg IV	27	264	$2s 2p^5(^3P^\circ)3p^4 S$
Mg V	43	311	$2s^2 2p^3(^2P^\circ)6p^1 D$
Mg VI	40	270	$2s 2p^3(^1D^\circ)3d^2 S^\circ$
Mg VII	47	260	$2s 2p^2(^2D)4p^1 P^\circ$
Mg VIII	43	190	$2s^2 8g^2 G$
Mg IX	74	242	$2s 30w^1 W$
Mg X	25	74	$30w^2 W$
Mg XI	1	1	
Al III	31	80	$30w^2 W$
Al IV	41	97	$2s^2 2p^5(^2P^\circ)6f^3 F$
Al V	48	170	$2s^2 2p^4(^3P)6d^2 D$
Al VI	44	305	$2s^2 2p^3(^4S^\circ)10f^3 F$
Al VII	65	254	$2s^2 2p^2(^3P)6f^2 D^\circ$
Al VIII	52	273	$2s^2 2p 6f^1 D$
Al IX	34	135	$2s^2 6g^2 G$
Al X	45	94	$2s 6f^1 F^\circ$
Al XI	25	75	$30w^2 W$
Al XII	1	1	
Si IV	37	48	$10f^2 F^\circ$
Si V	33	71	$2p^5 5f^3 F$
Si VI	42	132	$2s^2 2p^4(^3P)5d^2 D$
Si VII	34	151	$2s^2 2p^3(^2P^\circ)4f^1 G$
Si VIII	37	194	$2s^2 2p^2(^3P)5f^2 F^\circ$
Si IX	47	215	$2s^2 2p 5f^1 D$
Si X	44	204	$2s 2p(^1P^\circ)4f^2 D$
Sk XI	1	1	
P IV	36	178	$3p 5p^3 P$
P V	16	62	$10g^2 G$
P VI	1	1	
S III	13	28	$3s^2 3p 4s^1 P^\circ$
S IV	51	142	$3s^2 8z^2 Z$
S V	31	98	$3p 4d^1 P^\circ$
S VI	28	58	$10z^2 Z$
S VII	36	207	$2s^2 2p^5 10g^3 G^\circ$
S VIII	41	172	$2s^2 2p^4(^3P)6f^2 D^\circ$
S IX	44	233	$2s^2 2p^3(^4S^\circ)6f^3 F$
S X	34	72	$2s^2 2p^2(^1S)3d^2 D$
S XI	1	1	
Cl IV	40	129	$3p^3 3d(a)^3 D^\circ$
Cl V	26	80	$6s^2 S$
Cl VI	18	44	$3s 4f^1 F^\circ$
Cl VII	37	48	$10z^2 Z$
Cl VIII	1	1	
Ar III	10	36	$3s^2 3p^3(^2P^\circ)3d^3 P^\circ$
Ar IV	31	105	$3s^2 3p^2(^3P)4f^4 F^\circ$
Ar V	38	99	$3s^2 3p 5p^1 P$
Ar VI	21	81	$3s^2 5f^2 F^\circ$
Ar VII	30	72	$3p 4f^3 D$
Ar VIII	28	52	$10z^2 Z$
Ar IX	1	1	
Ca IV	31	137	$3s^2 3p^4(^3P)5g^2 F$
Ca V	43	107	$3s^2 3p^3(^2P^\circ)4d^1 F^\circ$
Ca VI	40	127	$3s^2 3p^2(^3P)5s^4 P$

Table 3 continued on next page

Table 3 (*continued*)

Species	N_S	N_F	Level name ^a
Ca VII	48	288	3s 3p ² (⁴ P)5p ³ P ^o
Ca VIII	45	296	3s 3d 4p ² Fb ^o
Ca IX	39	162	3s.7p ³ P ^o
Ca X	27	59	10f ² F ^o
Ca XI	32	150	2s ² 2p ⁵ 6d ¹ F ^o
Ca XII	1	1	
Cr IV	29	234	3d ² (³ P)5p ⁴ P ^o
Cr V	30	223	3d 6p ¹ F ^o
Cr VI	30	215	3p ⁵ 3d(¹ P)4s ² P ^o
Cr VII	1	1	
Mn IV	39	464	3d ³ (⁴ P)5p ⁵ S ^o
Mn V	16	80	3d ² (¹ S)4p ² P ^o
Mn VI	23	181	3d 4f ³ Pb ^o
Mn VII	20	203	10p ² P ^o
Mn VIII	1	1	
Fe IV	53	314	3d ⁴ (¹ D1)4p ² D ^o
Fe V	61	300	3d ³ (⁴ F)5s ⁵ F
Fe VI	44	433	3p ⁵ (² P)3d ⁴ (¹ S) ² Pc ^o
Fe VII	29	153	3p ⁵ (² P)3d ³ (b ² D) ¹ P ^o
Fe VIII	53	324	3p ⁵ 3d(b ³ D)4s ⁴ D ^o
Fe IX	52	490	(³ P)3d(⁴ P)5p ³ S ^o
Fe X	43	210	3s ² 3p ² 3d ³ (b) ⁴ P
Fe XI	72	1154	3s 3p ⁴ (⁴ P)7d ⁵ D
Fe XII	69	915	3s 3p ³ (⁵ S ^o)9f ⁶ F
Fe XIII	72	819	3s 3p ² (⁴ P)9g ⁵ G
Fe XIV	48	669	3s 3p(¹ P ^o)8f ² F
Fe XV	1	1	
Ni IV	36	200	3d ⁶ (³ D)4p ² D ^o
Ni V	46	183	3d ⁵ (² D3)4p ³ F ^o
Ni VI	37	314	3d ⁴ (⁵ D)4d ⁴ F
Ni VII	37	308	3d ³ (² D)4d ³ P
Ni VIII	34	325	3d ² (¹ G)4d ² D
Ni IX	34	363	3p ⁵ (² P)3d ² (¹ D)4p ¹ F
Ni X	1	1	

^aThe level name given here is the highest level included. Generally LS naming is used, but in some case identifiers have been added to distinguish levels with identical names. W states are used for states summed over all l -levels, but different multiplicities are kept separate. Z states are high l stats (e.g. g and higher) that have been combined into a single level in the model ion. In the model atoms high level terms are generally treated as single level, but lower terms are split.

REFERENCES

- Aggarwal, K. M., & Keenan, F. P. 2003, *A&A*, 399, 799
- . 2005, *A&A*, 429, 1117
- Allard, N., Le Dourneuf, M., Artru, M.-C., & Lanz, T. 1991, *A&AS*, 91, 399
- Asplund, M., Grevesse, N., & Sauval, A. J. 2005, in *Astronomical Society of the Pacific Conference Series*, Vol. 336, *Cosmic Abundances as Records of Stellar Evolution and Nucleosynthesis*, ed. I. Barnes, Thomas G. & F. N. Bash, 25
- Asplund, M., Grevesse, N., Sauval, A. J., & Scott, P. 2009, *ARA&A*, 47, 481

Table 4. Comparison between small and intermediate atomic models

Species	N_S/N_F	Level name	N_S/N_F	Level name
		“Small” model	“Intermediate” model	
C v	43/107	$2s^2 30w^1W$	43/107	$1s 30w^1W$
C vi	1/1		30/75	$30w^2W$
C vii			1/1	
O v	75/152	$2s 7f^1F^o$	82/234	$2s 30w^1W$
O vi	41/47	$12z^2Z$	59/ 65	30
Ne vi	36/202	$2s^2 10z^2Z$	59/239	$2s 2p(^3P^o)6d^4P^o$
Na iii	25/144	$2p^4(^3P)6f^2D^o$	25/145	$2p^4(^3P)6f^2D^o$
Mg iv	27/ 264	$2s 2p^5(^3P^o)3p^4S$	27/264	$2s^2 2p^4(^1D)7d^2S$
Al vii	65/254	$2s^2 2p^2(^3P)6f^2D^o$	68/289	$2s^2 2p^2(^3P)7p^4S^o$
Fe ix	52/490	$(^3P)3d(^4P)5p^3S^o$	59/712	$3s^2 3p^5(^2P)9k^3Ib$
Fe x	43/210	$3s^2 3p^2 3d^3(b)^4P$	115/1368	$3s 3p^5(^3P^o)5f^2F$
Fe xi	72/1154	$3s 3p^4(^4P)7d^5D$	118/1236	$3s 3p^4(^4P)7f^5F^o$
Fe xii	69/915	$3s 3p^3(^5S^o)9f^6F$	144/912	$3s 3p 3d^3(a)^2P^o$
Fe xiii	72/819	$3s 3p^2(^4P)9g^5G$	115/1239	$3s 3p^2(^4P)9g^5G$
Fe xiv	48/669	$3s 3p(^1P^o)8f^2F$	64/739	$3s^2 7h^2H^o$
Fe xv	1/ 1		64/448	$3d 6g^3F$
Fe xvi			20/77	$2p^6 30w^2W$
Fe xvii			1/1	
Ni v	46/183	$3d^5(^2D3)4p^3F^o$	152/1000	$3d^4(^1I)4s^2^1I$
Ni vi	37/314	$3d^4(^5D)4d^4F$	62/1000	$3d^4(^3D)4f^2Gb^o$
Ni vii	37/308	$3d^3(^2D)4d^3P$	61/1000	$3d^3(^4F)6p^3F^o$
Ni viii	34/325	$3d^2(^1G)4d^2D$	48/ 1000	$3p^5(^2P)3d^3(^2H)4s^4G^o$
Ni x	1/1		56/324	$3p^5 3d(b^3D)4s^4D^o$
Ni xi	1/1		89/499	$3s^2 3p^5(^2P)6h^3Gb$
Ni xii	1/1		46/233	$3s^2 3p^4(^3P)4f^2D^o$
Ni xiii	1/1		73/1236	$3s 3p^4(^4P)7f^5F^o$
Ni xiv	1/1		80/912	$3s 3p 3d^3(a)^2P^o$
Ni xv	1/1		122/1239	$3s 3p^2(^4P)9g^5G$
Ni xvi	1/1		48/669	$3s 3p(^1P^o)8f^2F$
Ni xvii			1/1	

Barlow, M. J., & Hummer, D. G. 1982, in IAU Symposium, Vol. 99, Wolf-Rayet Stars: Observations, Physics, Evolution, ed. C. W. H. De Loore & A. J. Willis, 387–392

Barniske, A., Hamann, W. R., & Gräfener, G. 2006, in Astronomical Society of the Pacific Conference Series, Vol. 353, Stellar Evolution at Low Metallicity: Mass Loss, Explosions, Cosmology, ed. H. J. G. L. M. Lamers, N. Langer, T. Nugis, & K. Annuk, 243

Bartzakos, P., Moffat, A. F. J., & Niemela, V. S. 2001, MNRAS, 324, 18

Berrington, K. A., Burke, P. G., Dufton, P. L., & Kingston, A. E. 1985, Atomic Data and Nuclear Data Tables, 33, 195

Burgess, A., & Summers, H. P. 1969, ApJ, 157, 1007

Butler, K., Mendoza, C., & Zeippen, C. J. 1993, Journal of Physics B Atomic Molecular Physics, 26, 4409

Cardelli, J. A., Clayton, G. C., & Mathis, J. S. 1989, ApJ, 345, 245

Castor, J. I., Abbott, D. C., & Klein, R. I. 1975, ApJ, 195, 157

Chen, G. X., & Pradhan, A. K. 1999, A&AS, 136, 395

Cochrane, D. M., & McWhirter, R. W. P. 1983, PhyS, 28, 25

Conti, P. S. 1976, Societe Royale des Sciences de Liege Memoires, 9, 193

Cox, A. N. 2000, Allen’s Astrophysical Quantities (New York: Springer)

Crowther, P. A., Dessart, L., Hillier, D. J., Abbott, J. B., & Fullerton, A. W. 2002, A&A, 392, 653

Cunto, W., Mendoza, C., Ochsenbein, F., & Zeippen, C. J. 1993, A&A, 275, L5

Davey, A. R., Storey, P. J., & Kisielius, R. 2000, A&AS, 142, 85

Ekström, S., Georgy, C., Eggenberger, P., et al. 2012, A&A, 537, A146

Eldridge, J. J., Stanway, E. R., Breivik, K., et al. 2020, MNRAS, 495, 2786, doi: [10.1093/mnras/staa1324](https://doi.org/10.1093/mnras/staa1324)

Eldridge, J. J., Stanway, E. R., Xiao, L., et al. 2017, PASA, 34, e058

Foellmi, C., Moffat, A. F. J., & Guerrero, M. A. 2003a, MNRAS, 338, 1025

—. 2003b, MNRAS, 338, 360

Table 5. Additional ions in largest model

Species	N_S	N_F	Level name
Ar IX	26	247	$2s^2 2p^5 10g \ ^3G^\circ$
Ar X	32	315	$2s^2 2p^4(^1S)8s \ ^2S$
Ar XI	1	1	
K III	20	40	$3p^4(^1S)3d \ ^2D$
K IV	40	612	$3p^3(^2D^\circ)10h \ ^1G$
K V	36	305	$3s 3p^3(^3P)4d \ ^2D^\circ$
K VI	54	513	$3s 3p^2(^4P)7p \ ^5S^\circ$
K VII	48	205	$3s 3p(^3P^\circ)6d \ ^4P^\circ$
K VIII	35	85	$3d 4s \ ^3D$
K IX	22	72	$30w \ ^2W$
K X	27	247	$2s^2 2p^5 10g \ ^1G^\circ$
K XI	32	315	$2s^2 2p^4(^1S)8s \ ^2S$
K XII	1	1	
Cr VII	52	712	$3s^2 3p^5(^2P)9k \ ^3Ib$
Cr VIII	43	1368	$3s 3p^5(^3P^\circ)5f \ ^2F$
Cr IX	109	1236	$3s 3p^4(^4P)7f \ ^5F^\circ$
Cr X	71	912	$3s 3p 3d^3(a) \ ^2P^\circ$
Cr XI	113	1239	$3s 3p^2(^4P)9g \ ^5G$
Cr XII	61	739	$3s^2 7h \ ^2H^\circ$
Cr XIII	62	448	$3d 6g \ ^3F$
Cr XIV	21	77	$2p^6 30w \ ^2W$
Cr XV	1	1	
Ni IX	48	1217	$4s 4d \ ^1D$

- Galavis, M. E., Mendoza, C., & Zeppen, C. J. 1997, *A&AS*, 123, 159
- Georgy, C., Ekström, S., Meynet, G., et al. 2012, *A&A*, 542, A29
- Gräfener, G., & Hamann, W. R. 2005, *A&A*, 432, 633
- Grafener, G., Hamann, W. R., Hillier, D. J., & Koesterke, L. 1998, *A&A*, 329, 190
- Gräfener, G., Koesterke, L., & Hamann, W. R. 2002, *A&A*, 387, 244
- Gräfener, G., Owocki, S. P., & Vink, J. S. 2012, *A&A*, 538, A40
- Grassitelli, L., Langer, N., Grin, N. J., et al. 2018, *A&A*, 614, A86
- Hainich, R., Rühling, U., Todt, H., et al. 2014, *A&A*, 565, A27
- Hamann, W. R., & Gräfener, G. 2004, *A&A*, 427, 697
- Hamann, W. R., & Schmutz, W. 1987, *A&A*, 174, 173
- Higgins, E. R., Sander, A. A. C., Vink, J. S., & Hirschi, R. 2021, *MNRAS*, 505, 4874, doi: [10.1093/mnras/stab1548](https://doi.org/10.1093/mnras/stab1548)
- Hillier, D. J. 1989, *ApJ*, 347, 392
- Hillier, D. J. 1991a, in *IAU Symposium*, Vol. 143, Wolf-Rayet Stars and Interrelations with Other Massive Stars in Galaxies, ed. K. A. van der Hucht & B. Hidayat, 59
- . 1991b, *A&A*, 247, 455
- Hillier, D. J. 2003, in *A Massive Star Odyssey: From Main Sequence to Supernova*, ed. K. van der Hucht, A. Herrero, & C. Esteban, Vol. 212, 70
- Hillier, D. J. 2012, in *From Interacting Binaries to Exoplanets: Essential Modeling Tools*, ed. M. T. Richards & I. Hubeny, Vol. 282, 229–234
- Hillier, D. J. 2015, in *Wolf-Rayet Stars*, ed. W.-R. Hamann, A. Sander, & H. Todt, 65–70
- Hillier, D. J., Aadland, E., Massey, P., & Morrell, N. 2021, *MNRAS*, 503, 2726
- Hillier, D. J., & Miller, D. L. 1998, *ApJ*, 496, 407
- . 1999, *ApJ*, 519, 354
- Howarth, I. D. 1983, *MNRAS*, 203, 301
- Humphreys, R. M., & McElroy, D. B. 1984, *ApJ*, 284, 565
- Husser, T. O., Wende-von Berg, S., Dreizler, S., et al. 2013, *A&A*, 553, A6
- Ishii, M., Ueno, M., & Kato, M. 1999, *PASJ*, 51, 417
- Kaur, J., Gorczyca, T. W., & Badnell, N. R. 2018, *A&A*, 610, A41
- Kramida, A. E., Ralchenko, Y., Reader, J., & NIST ASD Team. 2012, *NIST Atomic Spectra Database* (version 5.0). <http://physics.nist.gov/asd>
- Kudritzki, R. P., & Simon, K. P. 1978, *A&A*, 70, 653

- Kurucz, R. L. 2009, in American Institute of Physics Conference Series, Vol. 1171, American Institute of Physics Conference Series, ed. I. Hubeny, J. M. Stone, K. MacGregor, & K. Werner, 43–51
- Kurucz, R. L. 2010. <http://kurucz.harvard.edu/>
- Langer, N. 1989, *A&A*, 210, 93
- Lanz, T., & Hubeny, I. 2007, *ApJS*, 169, 83
- Leibowitz, E. M. 1972, *Journal of Quantitative Spectroscopy and Radiative Transfer*, 12, 299
- Lennon, D. J., & Burke, V. M. 1994, *A&AS*, 103, 273
- Lépine, S., & Moffat, A. F. J. 1999, *ApJ*, 514, 909
- Liang, G. Y., & Badnell, N. R. 2011, *A&A*, 528, A69
- Liang, G. Y., Whiteford, A. D., & Badnell, N. R. 2009, *Journal of Physics B Atomic Molecular Physics*, 42, 225002
- Lucy, L. B. 2007, *A&A*, 474, 701
- Luo, D., & Pradhan, A. K. 1989, *Journal of Physics B Atomic Molecular Physics*, 22, 3377
- Luo, D., Pradhan, A. K., Saraph, H. E., Storey, P. J., & Yu, Y. 1989, *Journal of Physics B Atomic Molecular Physics*, 22, 389
- Marshall, J. L., Burles, S., Thompson, I. B., et al. 2008, in *Proc. SPIE*, Vol. 7014, *Ground-based and Airborne Instrumentation for Astronomy II*, 701454
- Massey, P. 1981, *ApJ*, 246, 153
- Massey, P., Neugent, K. F., Hillier, D. J., & Puls, J. 2013, *ApJ*, 768, 6
- Massey, P., Neugent, K. F., Morrell, N., & Hillier, D. J. 2014, *ApJ*, 788, 83
- Massey, P., Olsen, K. A. G., Hodge, P. W., et al. 2007, *AJ*, 133, 2393
- McCandliss, S. R. 1988, PhD thesis, Colorado Univ., Boulder.
- Mendoza, C. 1983, in *IAU Symposium*, Vol. 103, *Planetary Nebulae*, ed. D. R. Flower, 143–172
- Moffat, A. F. J., Drissen, L., Lamontagne, R., & Robert, C. 1988, *ApJ*, 334, 1038
- Nahar, S. N. 1998, *PhRvA*, 58, 3766
- Nahar, S. N. 2010. http://www.astronomy.ohio-state.edu/~nahar/nahar_radiativeatomdata10/1086x101233
- Nahar, S. N., & Pradhan, A. K. 1993, *Journal of Physics B Atomic Molecular Physics*, 26, 1109
- Najarro, F., Hillier, D. J., & Stahl, O. 1997, *A&A*, 326, 1117
- Neugent, K. F., & Massey, P. 2014, *ApJ*, 789, 10
- Neugent, K. F., Massey, P., & Morrell, N. 2018, *ApJ*, 863, 181
- Nugis, T., & Lamers, H. J. G. L. M. 2002, *A&A*, 389, 162
- Nussbaumer, H., & Storey, P. J. 1979a, *A&A*, 74, 244
- . 1979b, *A&A*, 71, L5
- . 1983, *A&A*, 126, 75
- . 1984, *A&AS*, 56, 293
- Owocki, S. P., Castor, J. I., & Rybicki, G. B. 1988, *ApJ*, 335, 914
- Paczyński, B. 1967, *AcA*, 17, 355
- Pauldrach, A., Puls, J., & Kudritzki, R. P. 1986, *A&A*, 164, 86
- Peach, G., Saraph, H. E., & Seaton, M. J. 1988, *Journal of Physics B Atomic Molecular Physics*, 21, 3669
- Pietrzyński, G., Graczyk, D., Gallenne, A., et al. 2019, *Nature*, 567, 200
- Robert, C. 1994, *Ap&SS*, 221, 137
- Sana, H., de Mink, S. E., de Koter, A., et al. 2012, *Science*, 337, 444
- Sander, A., Hamann, W. R., & Todt, H. 2012, *A&A*, 540, A144
- Sander, A., Shenar, T., Hainich, R., et al. 2015, *A&A*, 577, A13
- Sander, A. A. C., Hamann, W. R., Todt, H., et al. 2019, *A&A*, 621, A92
- Sander, A. A. C., Vink, J. S., & Hamann, W. R. 2020, *MNRAS*, 491, 4406
- Schmutz, W., Hamann, W. R., & Wessolowski, U. 1989, *A&A*, 210, 236
- Schootemeijer, A., & Langer, N. 2018, *A&A*, 611, A75, doi: [10.1051/0004-6361/201731895](https://doi.org/10.1051/0004-6361/201731895)
- Seaton, M. J. 1987, *Journal of Physics B Atomic Molecular Physics*, 20, 6363
- Shaviv, N. J. 2001, *ApJ*, 549, 1093
- Shenar, T., Sablowski, D. P., Hainich, R., et al. 2020, *A&A*, 641, C2, doi: [10.1051/0004-6361/201935684e](https://doi.org/10.1051/0004-6361/201935684e)
- Simcoe, R. A., Burgasser, A. J., Schechter, P. L., et al. 2013, *PASP*, 125, 270
- Stafford, R. P., Bell, K. L., & Hibbert, A. 1994, *MNRAS*, 266, 715
- Stevance, H., Eldridge, J., & Stanway, E. 2020, *The Journal of Open Source Software*, 5, 1987
- Tayal, S. S. 2008, *A&A*, 486, 629
- Torres, A. V., & Massey, P. 1987, *ApJS*, 65, 459, doi: [10.1086/191233](https://doi.org/10.1086/191233)
- Träbert, E., Gwinner, G., Knystautas, E. J., Tordoir, X., & Wolf, A. 1999, *Journal of Physics B Atomic Molecular Physics*, 32, L491
- Tramper, F., Straal, S. M., Sanyal, D., et al. 2015, *A&A*, 581, A110
- Tully, J. A., Seaton, M. J., & Berrington, K. A. 1990, *Journal of Physics B Atomic Molecular Physics*, 23, 3811
- van den Bergh, S. 2000, *The Galaxies of the Local Group*
- van der Hucht, K. A. 2001, *NewAR*, 45, 135
- van Regemorter, H. 1962, *ApJ*, 136, 906

- Zhang, H. L., Graziani, M., & Pradhan, A. K. 1994, *A&A*,
283, 319
- Zhang, H. L., & Pradhan, A. K. 1997, *A&AS*, 126, 373

